Olfactory Navigation: Analysis of Simple Strategies and Animal Behavior

Nour Riman

May 2022

Neuroscience Institute

Dietrich College of Humanities and Social Sciences

Carnegie Mellon University

Pittsburgh, PA 15213

Submitted in partial fulfillment of the requirements

for the degree of Doctor of Philosophy

CARNEGIE MELLON UNIVERSITY

Thesis Committee:

Bard Ermentrout, Ph.D, Department of Mathematics, University of Pittsburgh

Claire Cheetham, Ph.D, Department of Neurobiology, University of Pittsburgh

Brent Doiron, Ph.D, Departments of Neurobiology and Statistics, University of Chicago

Jonathan D. Victor, Ph.D, M.D., Brain and Mind Research Institute and Department of Neurology, Weill Cornell Medical College

Olfactory Navigation: Analysis of Simple Strategies and Animal Behavior

Nour Riman

Carnegie Mellon University, 2022

Navigation is one of the most essential behaviors for animal survival. To navigate their worlds, animals use sensory cues that provide them with spatial information about their current location, and the direction and distance they should choose to travel to the next location. Information from olfactory cues and how they guide animal navigation remain a challenging problem to be studied. This is due to a difficulty in characterizing the physical properties of odor plumes that are temporally complicated and turbulent. Also, the neural circuits implicated in odor perception and its translation into olfactory driven motor behavior are still unclear and not easily understood. Studies have shown that animals employ different strategies to localize odor sources and follow odor trails. In this thesis, we study how animals use bilateral olfactory information in navigating their environment. We start by a mathematical analysis of the dynamics of a bilateral model that depends on the simultaneous comparison between odor concentrations detected by left and right sensors. We show that the animal has to be in an attraction region around the odor source in order to navigate towards the point source or follow the trail. We then introduce stochasticity into the bilateral model and study the effect of noise on the probability of finding an odor source. We find that constant noise is more successful when paired with a nonlinear function applied either to the concentration detected by the left and right sensors or to the difference in concentrations. We also show that concentration dependent noise improves performance for a spot source. Finally, we examine behavioral patterns of mice following odor trails in an attempt to assess whether bilateral olfactory cues are utilized by mice for navigation.

Acknowledgements

My path has been tortuous but I am finally here. It would not have been possible without the many people that have always been with me and those who I met along the way, so it would be remiss not to thank them all. First and foremost, my advisor Bard Ermentrout whose guidance and support pushed me forward and pulled me out of my own anxious mind. Bard is a great professor whose classes I have enjoyed immensely. He is the awesome researcher that I aspire to be. He is always curious and energized while working which inspires anyone who knows him to emulate him. His fun personality has made PhD life much more tolerable especially during a pandemic, granted that I will never get his music references. I also want to thank my committee members: Dr. Claire Cheetham, Dr. Brent Doiron, and Dr. Jonathan Victor for their time and help.

I am grateful to my friends from back home and those I met in Pittsburgh who have made time here much easier.

I am and will always be indebted to my family. I am forever grateful to my parents who have worked hard to provide me with the best education. My mother is the best person I know. She always put my sisters and me before her own self. I am thankful for all her sacrifices and prayers. My father's positive outlook and continuous encouragement have taught me to never give up and to press on no matter the difficulties. I am blessed to have two sisters who always support and motivate me. Their successes have inspired me and their ambition has fueled mine.

Table of Contents

List of Figures

1.0 Introduction

1.1 Olfaction

Animals use olfactory cues to navigate through their environment in order to find food [78, 11, 79], encounter mates [64, 59], avoid predators [39, 2, 19] and locate their home [24, 8, 68, 67]. This requires an ability to both localize odor sources and follow odor trails. How do animals utilize odor signals to extract directional cues in order to navigate to the source? What behavior allows for successful odor navigation and what are the algorithms that animals could be using?

1.2 Odor Landscape

Odorant molecules bind with olfactory receptor neurons causing their activation which mediates the sense of smell. The odorant diffuses or is transported by air or water. Turbulent advection and dispersion are the physical processes that transport odor signals. Odor plumes arise when the spatial structure of a chemical field is stirred due to dispersion and the change of velocity gradients in turbulent flows [50]. Odor plumes have a complex structure but it has been shown that the plumes disperse differently according to the landscapes they are in. If the odor is released in a freestream location far away from boundaries, the plume exhibits more intermittency, fluctuations and dilution of the concentration away from the source [18]. However, the plume has different spatiotemporal structure when released close to a boundary where it spreads laterally with little fluctuations [18, 33]. Photoionization detector (PID) [38] and planar laser-induced fluorescence (PLIF) [20, 73] have been used to measure odor plume structure. However, because of this complex and varying spatiotemporal structure, the concentration of the odor within the plumes is difficult to quantify and model.

1.3 Odor Sampling

To localize odor, animals have been observed to use serial sampling (klinotaxis) or bilateral sampling (tropotaxis) of the concentration [60]. Serial sampling depends on inter-sniff comparisons of odor concentrations between sequential sniffs that are measured at different locations. Bilateral sampling, on the other hand, depends on comparisons of odor concentrations detected by sensors located at two different positions of the body. It is not yet clear whether animals use one or more strategies that change according to the complexity of the environment, odor onset and loss [75], distance to the odor source or trail, or any other factor that affects their decision making. However, the distance to the odor source, and thus the steepness of concentration gradient, has been considered as one reason to switch strategies [15]. Due to the inter-naris distance restriction, Catania suggests that serial comparisons are better in shallower gradients - where larger movements provide directional information - while stereo comparisons are more useful near the odor source.

1.4 Stereo Olfaction

1.4.1 Stereo Olfaction in Insects

The ability to use inter-sensor geometry to localize odors has been observed in many animals especially insects. When one of the antennas was removed, walking fruit flies (*Drosophila melanogaster*) [9], flying fruit flies [26], ants (*Lasius fuliginosus*) [31] and honeybees (*Apis mellifera*) [47] showed a tendency to orient toward the intact side. Flying fruit flies were either slow to aquire a plume or unable to orient towards it when placed on the side of the occluded antenna. With crossed antennae, honeybees and ants constantly entered the scentfree arm of a Y tube. In larval chemotaxis [46], unilaterally functioning larvae were less accurate in sensing concentration gradient, an indication that integration between the left and right olfactory inputs increased the signal to noise ratio. In walking moths [70], the bombyx mori turned toward the side receiving stronger stimulus (intensity differences) or

larger latency (temporal differences). On the boundaries of the plume, they seemed to use bilateral inputs to decide the direction of turning. Within the plume, walking moths moved in a straight line with some fluctuation indicating that bilateral integration is important for source localization. Ants have also been observed to use stereo information not only to find food and follow pheromone but also to home [69].

1.4.2 Stereo Olfaction in Marine Animals

Marine animals have also shown dependence on bilateral information of the odor concentration to orient. Leopard sharks [53], which are nearshore species, followed more tortuous paths and ended farther away from the shore when one of their nostrils was blocked, in contrast to control sharks which ended closer to the shore with relatively straight tracks. Crustaceans also exhibited a loss of ability to correctly orient in an odor plume and efficiently find odor sources when one of their antennules was ablated [5, 23, 29, 44, 61].

1.4.3 Stereo Olfaction in Mammals

The detriment of loss of bilateral inputs was also shown in mammals. When one of the nostrils was partially or completely blocked, rats' accuracy in localizing odor dropped significantly and their response was biased towards the unblocked side. Their performance in tracking odor trails also declined and was less efficient [41, 60]. Blocking a nostril in moles also biased the animal in one direction and increased the latency to find the source [15]. In this study, crossing the airflow, by inserting polyethylene tubes into the nostrils, disrupted the ability to localize sources. Likewise, human subjects' accuracy almost halved when one nostril was taped during a scent tracking task [57]. Though humans could not report which nostril was receiving the stronger odor, their perceived direction was biased towards the higher concentration [80].

1.4.4 Neural Evidence of Stereo Olfaction

Recording from the olfactory bulb (OB) also lends evidence to the importance of bilateral inputs. It has been shown that half of the responsive neurons in the OB exhibited firing rate changes when odor was presented to one nostril and not the other [60]. Neurons in the anterior olfactory nucleus pars externa (AONpE) showed excitatory and inhibitory response to ipsilateral and contralateral nostril stimulation respectively [42]. The spike rate decreased accordingly when both nostrils were stimulated instead of only the ipsilateral nostril. The same was observed when an odor source was positioned more to the center of the nostrils than in the direction of the ipsilateral nostril. This suggests that AONpE neurons subtract the odor inputs and can detect position of odor sources relative to nostrils. AON was further shown to be both sufficient and necessary to trigger orientation responses [58]. In humans performing an odorant localization task, fMRI showed nostril specific neural activity in the left temporal piriform cortex [56].

1.5 Behavior and Strategies

Animals exhibit different behaviors while following odor trails or plumes. Upwind or upstream surge when odor is turned on has been observed in moths [65], walking flies [1], flying flies [72], and blue crabs [54]. Casting, which is characterized by zigzagging or crisscrossing, is also widely detected in animal behavior [72, 41, 40, 43]. It is expected that animals cast or zigzag in an attempt to find the plume or odor trail once they have lost it. However, if odor is sparse and therefore lost, the animals need to employ search strategies to find the plume before they can navigate it. Random walk models have been suggested as models of animal movements during foraging. To account for persistence in direction, correlated random walks and biased correlated random walks have been used [10, 17]. When resources are scarce or the environment to search is large, a Levy walk [81, 4] has been proposed as a search strategy that crosses larger areas and then concentrate its search in specific regions.

1.6 Thesis Outline

This thesis is organized into three parts that investigate strategies animals use to navigate. The second chapter aims to understand the role of bilateral information on its own in olfactory navigation. A bilateral model is presented that depends on the simultaneous comparison between odor concentrations detected by left and right sensors. After a mathematical analysis of the dynamics of the model, the behavior produced by this model is compared to previous animal data. This work, largely based on [62], indicates that the animal must be in a basin of attraction around the odor source in order to navigate towards the point source or follow the trail.

The third chapter addresses the effect of adding noise to the bilateral model which was introduced before. Performance is measured by examining the probability of success as nonlinear functions are applied to the concentrations and constant or concentration dependent noise is used. This work shows that stochastic resonance is observed such that an optimal level of noise is useful in improving the performance in finding odor sources which reflects on the importance of having a wide enough distribution of turning angles.

Finally, the fourth chapter examines the behavior of mice while they follow odor trails. The odor trails bifurcate into two branches at different angles. Body and nose positions of mice from many trials performing this task are extracted and analyzed. Then simulations of the strategy presented in the previous chapter are inspected and compared to the experimental data.

2.0 The Dynamics of Bilateral Olfactory Search and Navigation

2.1 Abstract

Animals use stereo sampling of odor concentration to localize sources and follow odor trails. We analyze the dynamics of a bilateral model that depends on the simultaneous comparison between odor concentrations detected by left and right sensors. The general model consists of three differential equations for the positions in the plane and the heading. When the odor landscape is an infinite trail, then we reduce the dynamics to a planar system whose dynamics have just two fixed points. Using an integrable approximation (for short sensors) we estimate the basin of attraction. In the case of a radially symmetric landscape, we again can reduce the dynamics to a planar system, but the behavior is considerably richer with multi-stability, isolas, and limit cycles. As in the linear trail case, there is also an underlying integrable system when the sensors are short. In odor landscapes that consist of multiple spots and trail segments, we find periodic and chaotic dynamics and characterize the behavior on trails with gaps and that turn corners.

2.2 Introduction

In this chapter, we present a mathematical analysis of tropotaxis in the presence of smooth odor sources and trails. We provide a fairly comprehensive analysis of the model dynamics, which in several cases reduces to a planar dynamical system. In the first section, we study the dynamics on an infinite trail. We show that there are always two stable fixed points and that there is an optimal sensor angle for attraction to the trail. We also show that the basin of attraction can be estimated from an associated integrable system. We next consider circularly symmetric trails which include a single spot as well as circular trails. The dynamics is more complicated there and we explore several different regimes including long sensors and sensors that are oriented behind the animal. Finally, we consider more

complicated odor landscapes such as partial trails and multiple odor sources. Here we also study trails with gaps and trails that branch and make sharp turns.

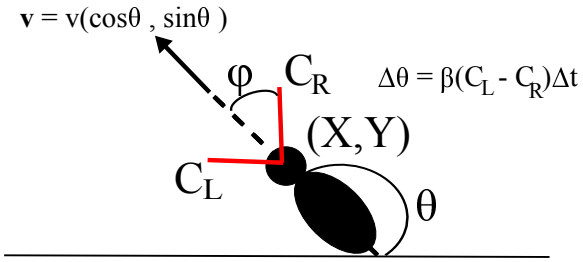

Figure 1: The bilateral model: an animal centered at (X, Y), heading in the direction, θ. The sensors are length, l with angle $\pm\phi$ around the axis of the body. Orientation is governed by the difference in concentrations at the two sensors, $C_L - C_R$ and speed is constant, v.

2.2.1 The Model

The model that we will analyze describes a navigation mechanism in which the angle of the heading (θ) of the individual depends on the difference between the concentration detected by the left and right sensors (See Fig. 1). The (X, Y) position of the individual is a function of the heading angle and the individual's speed v, which we will fix to be constant: the individual is always moving. The sensors have length l and are separated by an angle ϕ between them. They are located at the left and the right of the individual's body at positions $(X + l\cos(\theta + \phi), Y + l\sin(\theta + \phi))$ and $(X + l\cos(\theta - \phi), Y + l\sin(\theta - \phi))$ and detect odor concentration C_L and C_R where the concentration is generally a smooth gradient in some shape such as a line or a point source. The bilateral olfactory navigation model equations are

$$\begin{aligned}
\dot{X} &= v\cos\theta \\
\dot{Y} &= v\sin\theta \\
\dot{\theta} &= \beta\big[C_L(X, Y, \theta) - C_R(X, Y, \theta)\big].
\end{aligned}$$

The parameter β is the sensitivity to odor differences. If the concentration is greater on the left, the individual turns left and *vice versa.* To make the model dimensionless, we propose

a change of variables $(X, Y, t) \to (\sigma x, \sigma y, \frac{\sigma}{v}\hat{t})$ where σ is the spread of concentration and v is the velocity. This will change the left sensor position to $(x + \hat{l}\cos(\theta + \phi), y + \hat{l}\sin(\theta + \phi))$, the right sensor position to $(x + \hat{l}\cos(\theta - \phi), y + \hat{l}\sin(\theta - \phi))$, the sensor length to $\hat{l} = \frac{l}{\sigma}$, and the sensitivity to concentration difference to $\hat{\beta} = \frac{\sigma}{v}\beta$. The new model equations are

$$\begin{aligned} \dot{x} &= \frac{\partial x}{\partial \hat{t}} = \cos\theta \\ \dot{y} &= \frac{\partial y}{\partial \hat{t}} = \sin\theta \\ \dot{\theta} &= \frac{\partial \theta}{\partial \hat{t}} = \hat{\beta}\big[C_L(x,y) - C_R(x,y)\big]. \end{aligned} \tag{1}$$

These equations together with the initial conditions give us the bilateral model. We will use this dimensionless model throughout the chapter unless otherwise mentioned and we will drop the $\hat{}$ for easier notation.

2.3 Infinite Line

We will start by analyzing how the model performs when the odor is along an infinite line. This corresponds to a straight trail along the $y-$axis. Here, the object is for the individual to find the trail (i.e., navigate to it) and then keep on it. The odor concentration has a Gaussian profile and is equal to $C(x) = \exp(-x^2)$. (This is the simplification of a point source odor profile; one can use a more principled model based on advection-diffusion equation, c.f. [74] Eq. 6, supplement, but the Gaussian has the advantage of being smooth at the origin making the analysis possible. Results for other odor profiles are qualitatively similar.) Since the concentration is independent of y, the equations are reduced to a simple planar ODE:

$$\begin{aligned} \dot{x} &= \cos\theta \\ \dot{\theta} &= \beta\big[C_L(x) - C_R(x)\big]. \end{aligned}$$

where the sensors position are

$$x_L = x + l\cos(\theta + \phi)$$
$$x_R = x + l\cos(\theta - \phi)$$

The fixed points of the system are at $(0, \pm\frac{\pi}{2})$. They correspond to finding the trail and either going up $(+\pi/2)$ or down $(-\pi/2)$ the trail. Here, we will limit our domain to $\theta \in [0, \pi]$, and thus the fixed point is at $(0, \frac{\pi}{2})$. This fixed point is stable as long as $\phi \in (0, \pi/2)$, as is the corresponding fixed point at $-\pi/2$. Looking at the Jacobian:

$$J(x,\theta) = \begin{bmatrix} 0 & -\sin\theta \\ \beta(\frac{\partial C_L}{\partial x} - \frac{\partial C_R}{\partial x}) & \beta(\frac{\partial C_L}{\partial \theta} - \frac{\partial C_R}{\partial \theta}) \end{bmatrix}$$
$$\frac{\partial C_L}{\partial x} = -2(x + l\cos(\theta+\phi)\exp -(x + l\cos(\theta+\phi))^2$$
$$\frac{\partial C_R}{\partial x} = -2(x + l\cos(\theta-\phi)\exp -(x + l\cos(\theta-\phi))^2$$
$$\frac{\partial C_L}{\partial \theta} = 2(x + l\cos(\theta+\phi))l\sin(\theta+\phi)\exp -(x + l\cos(\theta+\phi))^2$$
$$\frac{\partial C_R}{\partial \theta} = 2(x + l\cos(\theta-\phi))l\sin(\theta-\phi)\exp -(x + l\cos(\theta-\phi))^2$$
$$J(0,\frac{\pi}{2}) = \begin{bmatrix} 0 & -1 \\ 4\beta l\sin(\phi)\exp(-(l\sin\phi)^2) & -2\beta l^2\sin(2\phi)\exp(-(l\sin\phi)^2) \end{bmatrix}$$

The trace and determinant of the linearization are respectively:

$$\begin{aligned} \text{Tr} &= -2\beta l^2\sin(2\phi)\exp(-(l\sin\phi)^2) \\ \text{Det} &= 4\beta l\sin(\phi)\exp(-(l\sin\phi)^2). \end{aligned}$$

Since the trace is negative and the determinant is positive for all $\phi \in (0, \pi/2)$, the fixed point is asymptotically stable. This fixed point shifts horizontally if the length of the sensors are not the same. It becomes a saddle point when the sensors are crossed and then the individual will not be able to navigate the odor trail. Also, the individual will not find the trail when one of its sensors is cut. The left panel of Fig. 2A shows a pair of trajectories, one of which misses the equilibrium and travels off to the right and another that eventually lands on the fixed point suggesting that there is a basin of attraction for the fixed point. The right panel of Fig. 2A shows the projection of these trajectories in $(x, y)-$plane. Fig. 2B

shows the basin of attraction for $l = 0.2, \phi = 1, \beta = 10, 1$ in solid red and blue respectively. (These curves are computed by integrating backwards starting at $x = \pm 5$ and θ close to $\pi/2$.) Any initial data contained within the solid curves will be attracted to the fixed point $(0, +\pi/2)$ and any initial data outside this will go off to $\pm\infty$. As would be expected, the blue region lies entirely in the red region. Intuitively, if the individual is too far away from the source, unless it is nearly aligned with the trail, the concentration difference will never get large enough to allow it to correct. We can put this intuition on a more rigorous footing by assuming the sensor length, l, is small to get (via Taylor's theorem):

$$\begin{aligned}
\lim_{l\to 0} \frac{C_L - C_R}{l} &= \lim_{l\to 0} \frac{1}{l}\Big[\exp -\big(x + l\cos(\theta+\phi)\big)^2 - \exp -\big(x + l\cos(\theta-\phi)\big)^2 \Big] \\
&= \lim_{l\to 0} \frac{\exp -(x^2)}{l}\Big[\exp\big(2lx\cos(\theta+\phi) - l^2\cos^2(\theta+\phi)\big) \\
&\qquad - \exp\big(-2lx\cos(\theta-\phi) - l^2\cos^2(\theta-\phi)\big)\Big] \\
&= \lim_{l\to 0} \frac{\exp -(x^2)}{l}\Big[-2xl\cos(\theta+\phi) - l^2\cos^2(\theta+\phi) + 2xl\cos(\theta-\phi) \\
&\qquad + l^2\cos^2(\theta-\phi) + \frac{1}{2}\big(-2lx\cos(\theta+\phi) - l^2\cos^2(\theta+\phi)\big)^2 \\
&\qquad - \frac{1}{2}\big(-2lx\cos(\theta-\phi) - l^2\cos^2(\theta-\phi)\big)^2 + ...\Big] \\
&= \exp -(x^2)\Big[-2x\cos(\theta+\phi) + 2x\cos(\theta-\phi)\Big] \\
&= 4x\exp -(x^2)\sin\theta\sin\phi.
\end{aligned}$$

Therefore, for small l, the difference between the concentrations detected by the left and right sensors is

$$C_L - C_R = [4l\sin\phi]\, x\exp(-x^2)\sin\theta + O(l^2)$$

so that we obtain an approximate system:

$$\begin{aligned}
\dot{x} &= \cos\theta \\
\dot{\theta} &= 4[\beta l\sin\phi]\, x\exp(-x^2)\sin\theta.
\end{aligned}$$

This ODE is integrable, with

$$E(x,\theta) := -2\beta l\sin\phi\exp(-x^2) - \log(|\sin\theta|) = \text{constant}.$$

$E(x, \theta) = 0$ corresponds to a pair of trajectories (shown by the dashed lines in figure 2B) that separate bounded ($E < 0$) from unbounded ($E > 0$) trajectories. As can be seen in the figure, these curves are reasonable approximations to the full basin of attraction (at least for l small).

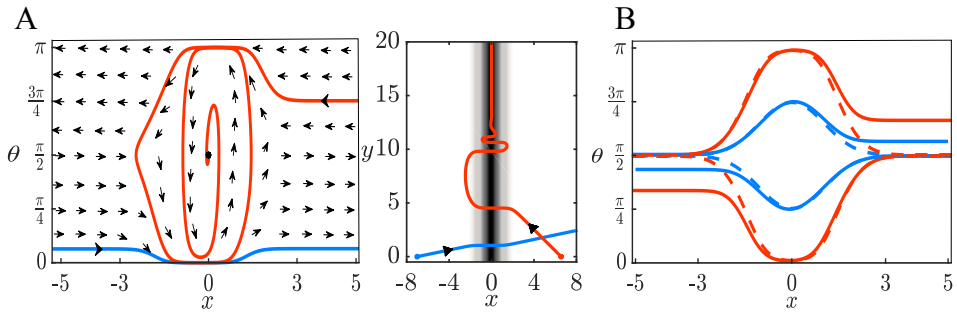

Figure 2: (A) (left) Phase plane when trail is an infinite line. One trajectory converges to the stable fixed point at $(0, \frac{\pi}{2})$ but another does not. From the vector field, a separatrix can be noticed around the line, $\theta = \pi/2$. (right) Projection of the solutions in the $(x, y)-$plane. (B) Basin of attraction of the trail. The dashed lines are the separatrices for the integrable system that separate the bounded solutions from the unbounded. The solid lines are the numerically simulated basins. The blue lines represent the basin when $\beta = 1$ and the red lines when $\beta = 10$ Here $\phi = 1, l = 0.2$.

2.3.1 Sensor angles

The sensor angles play an important role in the ability to find and follow a trail. Furthermore, they are something that can be under control of the animal, whereas sensitivity and sensor length would be difficult to vary. Fig. 3A shows the basin of attraction for a trail with $\beta = 10, l = 1$ as ϕ is varied from the nominal value, $\phi = 1$ to $\phi = 0.2, 1.5$ and $\phi = 0.57$ (the angle at which the trace is minimum for $l = 1$). Consider the upper part of the diagram (the bottom is similar under the transformation, $x \to -x, \theta \to \pi - \theta$). As ϕ increases toward $\pi/2$ (blue curve) and $x(0) > 0$, the individual must be more closely aligned with the trail ($\theta(0)$ closer to $\pi/2$). For $x(0) < 0$, the initial heading does not matter as long

as $x(0)$ is close enough to the trail and in this case, there is a slight advantage to increasing the angle. On the other hand, with small ϕ (black curve), there seems to be no difference from $\phi = 1$ for $x > 0$, but for $x < 0$ the basin is decreased. While we have not measured the precise area of the basin, it would appear that $\phi = 1$ (green) has the largest; losing a little for $x < 0$ but keeping the maximal amount for $x > 0$. We also note that when $\phi = 0.57$ (red), the basin is very close to that of $\phi = 1$.

The basin is impossible to compute analytically, but a plausible surrogate is the divergence of the vector field at the fixed point, $(x, \theta) = (0, \pi/2)$. We thus consider the trace of the linearization around the fixed point which was given above. We plot this quantity as a function of ϕ for several different values of l as shown in Fig. 3B. Clearly as l increases the minimum shifts toward lower values of ϕ. With a little bit of calculus and algebra, we find that

$$\cos\phi_{min} = \sqrt{\frac{l^2 + \sqrt{l^4+1} - 1}{2l^2}}.$$

We arrive at the result above by taking the derivative of the trace with respect to ϕ:

$$\frac{dTr}{d\phi} = -4\beta l^2 \cos(2\phi)\exp(-(l\sin\phi)^2) + 4\beta l^4 \sin(2\phi)\sin(\phi)\cos(\phi)\exp(-(l\sin\phi)^2) = 0$$

$$4\beta l^2 \exp(-(l\sin\phi)^2)\big(-\cos(2\phi) + l^2\sin(2\phi)\sin(\phi)\cos(\phi)\big) = 0$$

$$4\beta l^2 \exp(-(l\sin\phi)^2)\big(\sin^2(\phi) - \cos^2(\phi) + 2l^2\sin^2(\phi)\cos^2(\phi)\big) = 0.$$

Let $z = \cos^2\phi$, then solve for the quadratic equation

$$(1-z) - z + 2l^2(1-z)z = 0,$$

which will yield

$$z = \frac{l^2 - 1 + \sqrt{(1-l^2)^2 + 2l^2}}{2l^2} = \frac{l^2 - 1 + \sqrt{l^4+1}}{2l^2}.$$

Replacing $\sqrt{z} = \cos\phi$, we get the result.

The right hand side ranges between $1/\sqrt{2}$ and 1 as l ranges between 0 and ∞. This suggests that the sensors should have an angle between them that is between 0 and $\pi/2$. The distance between the sensors is $2l\sin\phi$, yielding the optimal distance to be:

$$d_{opt}(l) = \sqrt{2\,l^2 - 2\sqrt{l^4+1} + 2}.$$

d_{opt} saturates near $l = 2$ at $\sqrt{2}$, which suggests that the optimal sensor distance for staying on a trail whose characteristic width is σ will be $\sqrt{2}\sigma$.

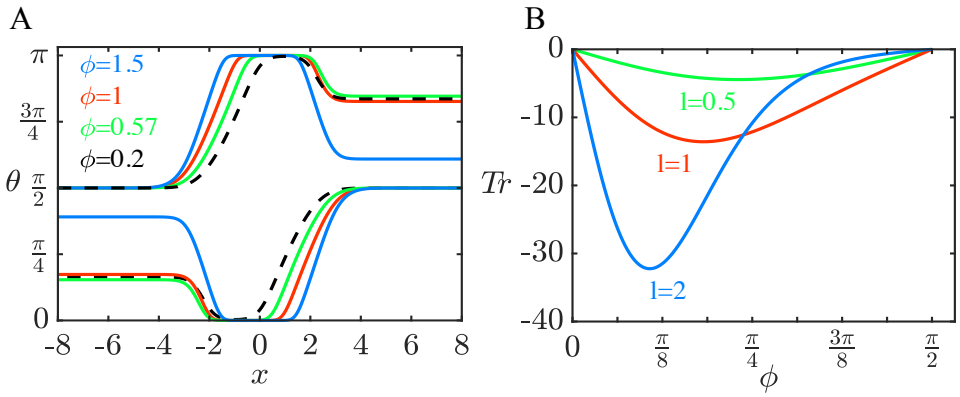

Figure 3: (A) Basin of attraction for the stable fixed point $(0, \pi/2)$ for trail following as a function of initial orientation and $x-$position for 4 different sensor angles, ϕ. Remaining parameters are $l = 1, \beta = 10$. (B) Trace of the linearization about the stable fixed point as the angle between the sensors varies.

In sum, a single infinite odor trail greatly simplifies the dynamics to lie on the plane. There are only two fixed points, both always stable corresponding to moving up or down the trail. There is an optimal angle for the sensors that maximizes the stability and decreases with the sensor length. The basin of attraction is well-approximated by a simple analytic formula for an associated integrable system.

2.4 Radially Symmetric Landscapes

We now turn our attention to odor landscapes that are radially symmetric, which include point sources and circular trails. This symmetry allows us to again reduce the three-dimensional dynamical system to a planar system. We introduce polar coordinates, r, ψ ($x = r\cos\psi, y = r\sin\psi$) and the relative coordinate, $\xi = \theta - \psi$. Note that $\xi = 0$ (respectively $\xi = \pi$) corresponds to heading away from (resp. toward) the source along a radial line

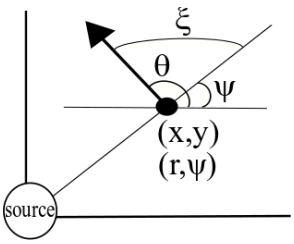

Figure 4: Change of variables when odor landscape is radially symmetric. (r, ψ) are the polar coordinates introduced when the individual is at position (x, y) and has a heading angle θ. ξ is the relative coordinate where $\xi = \theta - \psi$.

(See Fig. 4). Differentiating $x = r\cos\psi, y = r\sin\psi$,

$$\dot{x} = \dot{r}\cos\psi - \dot{\psi} r\sin\psi \tag{2}$$

$$\dot{y} = \dot{r}\sin\psi + \dot{\psi} r\cos\psi. \tag{3}$$

$(2)\cos\psi + (3)\sin\psi$ and $-(2)\sin\psi + (3)\cos\psi$ will give

$$\dot{r} = \dot{x}\cos\psi + \dot{y}\sin\psi = \big(\cos\theta\cos\psi + \sin\theta\sin\psi\big) = \cos(\theta - \psi)$$
$$\dot{\psi} = \frac{1}{r}\big(-\dot{x}\sin\psi + \dot{y}\cos\psi\big) = \frac{1}{r}\big(-\cos\theta\sin\psi + \sin\theta\cos\psi\big) = \frac{1}{r}\sin(\theta - \psi).$$

With these coordinates, we again obtain a planar system:

$$\begin{aligned} \dot{r} &= \cos\xi \\ \dot{\xi} &= \beta\big[C_L(r,\xi) - C_R(r,\xi)\big] - \frac{1}{r}\sin\xi := G(r,\xi). \end{aligned} \tag{4}$$

With a radially symmetric concentration, $C(r)$, the left and right concentrations are

$$C_L(r,\xi) = C\big(\sqrt{r^2 + l^2 + 2lr\cos(\xi + \phi)}\big)$$
$$C_R(r,\xi) = C\big(\sqrt{r^2 + l^2 + 2lr\cos(\xi - \phi)}\big).$$

Any equilibria will have $\xi = \pm\pi/2$ and $r = \bar{r}$ chosen to solve $G(\bar{r}, \pm\pi/2) = 0$. These fixed points correspond to the individual moving counter clockwise (resp. clockwise) around the

source at a constant velocity. Whether such fixed points exist and whether they are stable is the subject of the rest of this section.

Henceforth, we will assume the concentration has the form: $C(r) = \exp(-(r - r_0)^2)$ where the peak concentration forms a ring of radius r_0 around a central point. Note that $r_0 = 0$ is a point source. As noted above, there are two different values of ξ corresponding to equilibria; since they just represent the individual going clockwise or counter-clockwise, we will focus on the latter, $\bar{\xi} = \pi/2$.

Remark. We have chosen a simplistic model for the circular trail, $C(r, r_0) = \exp(-(r-r_0)^2)$ which is not a physical possibility. Rather, the correct form is to convolve the Gaussian with a Dirac distribution on a circle. The result of this is:

$$C_{real}(r, r_0) = N(r_0) I_0(2r_0 r) \exp(-2r_0 r) \exp(-(r - r_0)^2),$$

where I_0 is the modified Bessel function of the first kind and $N(r_0)$ is chosen so that $C_{real}(r, r_0)$ has a maximum value of 1. One problem is the computation of $N(r_0)$ since there is no simple analytical expression for the value of r maximizing C_{real}. For r_0 close to zero, the two forms are indistinguishable and for $r_0 > 2$, they are also quite close. Thus it is only for values of r_0 around 1 that there are differences. (Recall, that we have scaled the width of the Gaussian to be 1.) We have reproduced all the phase-portraits except those in Fig. 6 using the physically correct concentration. However, we also note that we have only approximated $N(r_0)$ as no analytic expression exists and the behavior in figure 6 occurs for a very limited range of r_0.

When $\xi = \pi/2$ (fixed point) and $r_0 = 0$ (odor is point source), the concentration difference becomes:

$$\begin{aligned} C_L - C_R &= exp(-r^2 - l^2 - 2rl\cos(\xi + \phi)) - exp(-r^2 - l^2 - 2rl\cos(\xi - \phi)) \\ &= exp(-r^2 - l^2)[exp(-2rl\cos(\xi + \phi)) - exp(-2rl\cos(\xi - \phi))]. \end{aligned}$$

To check the stability of the fixed point, we start by calculating the Jacobian matrix and then find the trace and determinant.

$$J(r, \xi) = \begin{bmatrix} 0 & -\sin\xi \\ \beta\frac{\partial(C_L - C_R)}{\partial r} + \frac{\sin\xi}{r^2} & \beta\frac{\partial(C_L - C_R)}{\partial \xi} - \frac{\cos\xi}{r} \end{bmatrix}$$

$$
\begin{aligned}
trace(J(r,\frac{\pi}{2})) &= \beta\frac{\partial(C_L - C_R)}{\partial\xi}|_{\xi=\pi/2} \\
&= \beta exp(-r^2-l^2)[2rl(\cos\phi)\exp(2rl\sin\phi) - 2rl(\cos\phi)\exp(-2rl\sin\phi)] \\
&= 2rl\beta(\cos\phi)\exp(-r^2-l^2)\sinh(2rl\sin\phi) \geq 0 \\
det(J(r,\frac{\pi}{2})) &= \frac{1}{r^2} + 2\beta\exp(-r^2-l^2)[l(\sin\phi)\cosh(2rl\sin\phi) - r\sinh(2rl\sin\phi)].
\end{aligned}
$$

So depending on $r > 0$, the determinant can be > 0 or < 0 and then the fixed points $(r, \frac{\pi}{2})$ are either an unstable fixed point or a saddle point.

Fig. 5A shows the behavior of the model when $r_0 = 0$, a point source. The top shows the phase-plane for (4). There are two fixed points, the one closest to $r = 0$ is an unstable source and the larger one is a saddle point. The stable (cyan) and unstable (orange) manifolds are drawn. While there are no attractors in this case, the stable manifolds still play an important role in the dynamics. If the initial data lies above them, then solutions in the (x, y, θ) system will pass through the odor spot as seen in the $(x, y)-$projection in the bottom of the panel. Initial data below the manifolds will veer off without getting closer to the spot. While there are no attractors (there is no "trail" to follow), from a practical point of view, any initial condition above the stable manifolds will "find" the spot. The bifurcation diagram in Fig. 5D shows the behavior of the small r fixed point as r_0 increases. At $r_0 \approx 0.5$, the unstable source becomes a stable sink via a Hopf bifurcation. A branch of unstable periodic orbits (blue curves) emerges and terminates at an orbit homoclinic with the saddle point (not shown). We remark that for large r_0, the stable equilibrium is $r \approx r_0$, so the individual is centered on the trail just as in the line trail. Fig. 5C top (bottom) panel shows the $(r, \xi)-$phaseplane ((x, y) projection) for $r_0 = 4$. In this case, the stable manifolds form the basin of attraction for the circular trail. Any initial condition starting within the basin will find and follow the trail (blue trajectories) while outside the basin will not follow it (red trajectories). Fig. 5B shows the $(r, \xi)-$phaseplane for $r_0 = 1$. In this case, the basin is the unstable periodic orbit that is the α-limit set of one of the branches of the stable manifold. If one of the sensors is cut, the individual converges to a new stable periodic orbit (in (x, y) plane) with a smaller radius as long as it is starting in the region bounded by the circular trail.

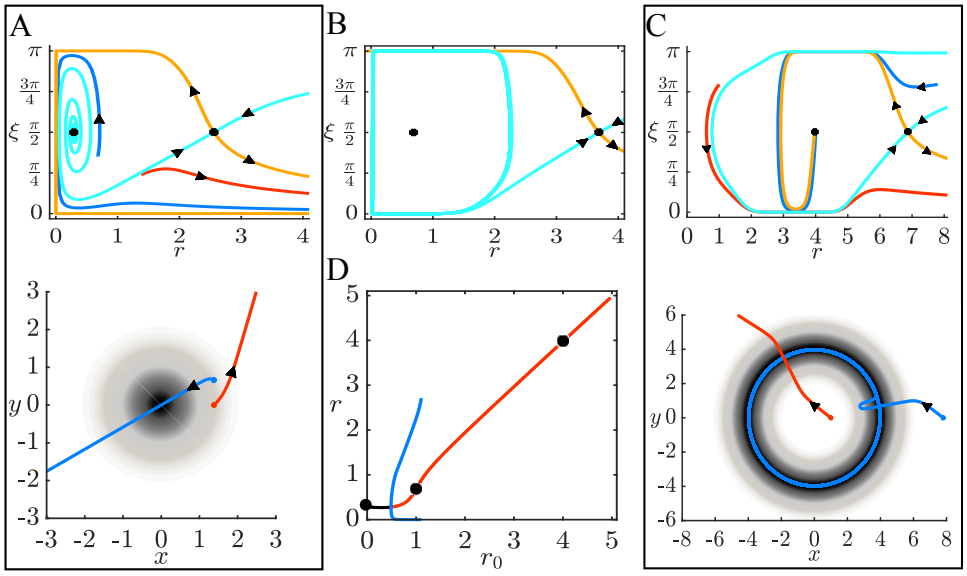

Figure 5: A. (top) Phaseplane for equation (4) for $r_0 = 0$, a spot source showing an unstable spiral (near $r = 0.4$) and a saddle (near $r = 2.5$) along with its stable (cyan) and unstable (orange) manifolds and two trajectories. (bottom) Projection of the solutions in the $(x, y)-$plane. (B) Phaseplane for $r_0 = 1$. The stable manifold forms an unstable limit cycle as shown in the bifurcation diagram, D. The fixed point inside is stable. C. (top) Phaseplane for $r_0 = 4$ with the same conventions as in panel A. Note the unstable spiral has become an attractor. (bottom) Projection in the $(x, y)-$plane. (D) Bifurcation diagram as a function of the trail radius, r_0; stable (unstable) fixed points are red (black) and unstable limit cycles are blue. Black dots correspond to $r_0 = 0, 1, 4$ and the phaseplanes in A,B,C. Parameters are $\beta = 10, \phi = 1, l = 1$.

2.4.1 Dependence on the model parameters

The stabilization of the fixed point as r_0 increases occurs via a Hopf bifurcation. In the next sections, we explore this dependence in detail.

2.4.1.1 Sensor angle

The sensor angle, ϕ provides an interesting picture. We first note that if we let $\hat{\phi} = \pi - \phi$ and $\hat{\xi} = \xi + \pi$, the concentrations become:

$$\begin{aligned} C_L(r,\hat{\xi}) &= exp(-(\sqrt{r^2+l^2+2lr\cos(\hat{\xi}+\hat{\phi})} - r_0)^2) \\ &= exp(-(\sqrt{r^2+l^2+2lr\cos(\xi-\phi)} - r_0)^2) = C_R(r,\xi) \\ C_R(r,\hat{\xi}) &= exp(-(\sqrt{r^2+l^2+2lr\cos(\hat{\xi}-\hat{\phi})} - r_0)^2) \\ &= exp(-(\sqrt{r^2+l^2+2lr\cos(\xi+\phi)} - r_0)^2) = C_L(r,\xi), \end{aligned}$$

and then equation (4) becomes:

$$\begin{aligned} \frac{dr}{dt} &= -\cos\hat{\xi} \\ \frac{d\hat{\xi}}{dt} &= -\left(\beta\big[C_L(r,\hat{\xi}) - C_R(r,\hat{\xi})\big] - \sin\hat{\xi}/r\right), \end{aligned}$$

with $\hat{\phi}$ replacing ϕ. Angles $\phi \in (\pi/2, \pi)$ correspond to the individual having its sensors behind it. This calculation shows that the vector field for $\phi \in (\pi/2, \pi)$ is the same as that for $\phi \in (0, \pi/2)$ in reverse time. Thus, for example, unstable periodic orbits for $\phi \in (0, \pi/2)$ become stable periodic orbits for $\phi \in (\pi/2, \pi)$. Additionally, note that when $\phi = \pi/2$, then Eq.(4) is a reversible system, since $\xi \to \xi + \pi$ takes $t \to -t$. Thus, for fixed r_0 and increasing ϕ from 0, there will be three Hopf bifurcations; the middle one is degenerate and is at $\phi = \pi/2$, the reversible system. To get more insight into the full dynamics, we look at the (ϕ, r_0) parameter plane in more detail. Fig. 6 shows bifurcation diagrams as ϕ varies for several different values of r_0. There are several notable features. The central diagram shows the curves of Hopf bifurcations (blue) in addition to curves of saddle-nodes of limit cycles (SNLCs, black). The latter curve is non-monotonic, so that there is a region (below the red dashed curve), where there can be two SNLCs. The lower right diagram shows that these

delineate an isola (isolated branch) of periodic orbits. As r_0 increases, this isola merges with the branch of unstable periodic orbits (lower left diagram). Between $r_0 = 0.51$ and $r_0 = 0.55$, the stable and unstable branches collide with the saddle at a saddle-homoclinic bifurcation (shown as H in the upper right diagram). Finally, the SNLC merges with the Hopf bifurcation curves (shown by the asterisk in the central figure) leaving an unstable periodic orbit (upper left diagram; the other unstable periodic orbit is not shown). The apparent existence of stable periodic orbits for small radii trails and small sensor angles implies that there is a stable torus in the full (x, y, θ) system.

2.4.1.2 Sensor length

Surprisingly, we have found multistability on circular trails of radius, r_0, for sensors that have the same approximate length $l \approx r_0$ and small attraction, β. Figure 7 shows some examples of the dynamics. Here, we choose $r_0 = 4$ and l between 4 and 6, while letting β range between 0.5 and 3.5. The dynamics is organized around the two parameter curves of various bifurcations (not all of them are shown, either for clarity or for inability to follow them). In the figure, curves of saddle-node bifurcations of equilibria (SNE) are shown in red, Hopf bifurcations in blue, and a homoclinic bifurcation in olive. Phaseplanes in some of the regions are shown. We emphasize once again, that stable fixed points (limit cycles) in this reduced system correspond to stable periodic orbits (tori) in the full three-dimensional model (See Fig. 8). Starting in region (a), there is a single attracting fixed point whose basin is delineated by the stable manifolds of the outer saddle. (As we will eventually encounter another saddle point, the outer one will be the one that is at roughly $r = 9$. It persists throughout the figure.) Two bifurcations occur as we move from a to b. First, there is a homoclinic bifurcation at the outer saddle leading to an unstable periodic orbit (UP) that plays the role of the basin for the fixed point. (This is not shown as a separate phaseplane since the attractor structure is still the same.) As we cross the red curve into region b, two new fixed points arise: a stable node and a saddle. The UP continues to provide the basin, but the stable manifolds of the inner saddle (near $r = 2$) split this basin between the two stable fixed points. Recalling that $r_0 = 4$, we see the outer fixed point shows the

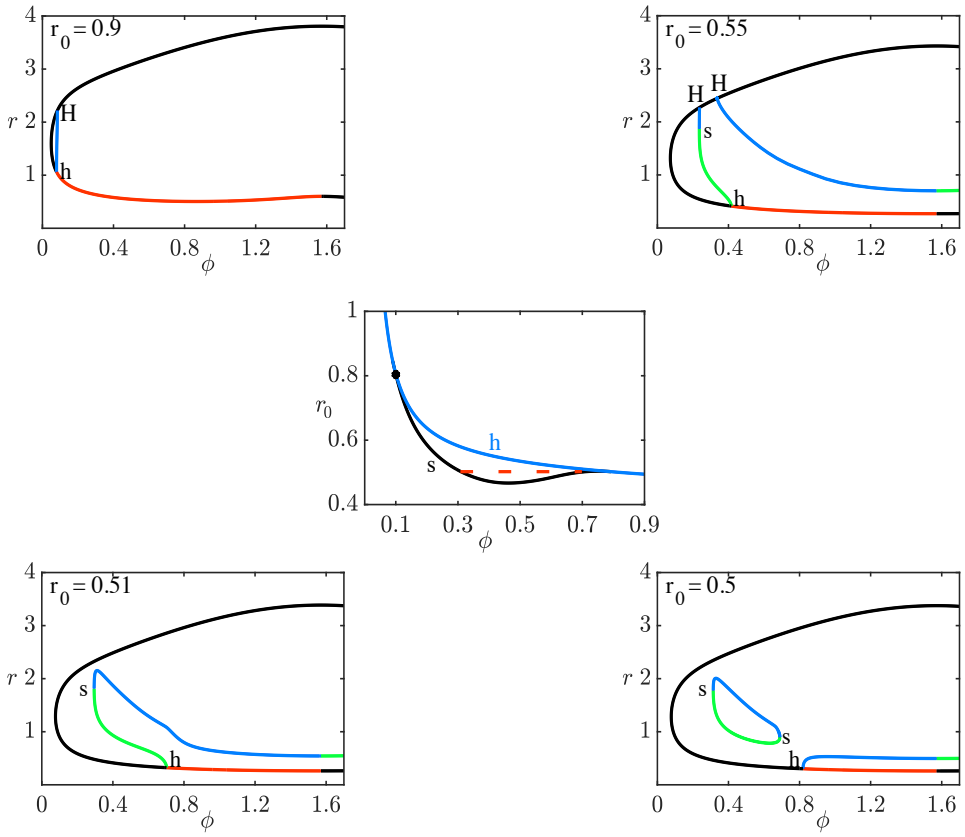

Figure 6: Behavior as r_0, ϕ vary. Center figure shows the two-parameter (ϕ, r_0) plane. Blue line denotes the curve of Hopf bifurcations. Above this curve there is a stable fixed point. The black line is the curve of saddle-node bifurcations of periodic orbits. Below the red dashed line there are 2 saddle-node of limit cycles (isola). One-parameter bifurcation diagrams are shown for different values of r_0 as ϕ varies. Black (Red):unstable (Stable) fixed points; Blue (Green): unstable (stable) periodic orbits. (h), Hopf bifurcations; (s), saddle-node of limit cycles; (H), saddle-homoclinic orbits.

individual following the trail while with the inner stable fixed point the individual makes smaller circles within the trail. In the transition from b to c, the inner fixed point undergoes a Hopf bifurcation and spawns a stable periodic orbit (SP). Thus, in the (x, y, θ) model there is bistability between the individual tracking the trail and a quasiperiodic trajectory that lies near the center of the trail. Fig. 8 shows the dynamics in the (x, y)-plane. The transition from c to d occurs through a homoclinic bifurcation (olive curve) where the SP disappears. The result is just a single attractor. In d to g, this attractor is lost via a SNE and there remain no attractors. The path from c to e occurs via a SNE leaving just a SP whose basin is determined by the UP. The transition from e to g occurs when the SP and the UP (SNLC) merge and disappear. The transition from e to f occurs when limit cycle disappears through a reverse Hopf bifurcation stabilizing the fixed point shown by the hollow square. Region f has only one attractor, this stabilized fixed point is near $r = 1$ and is not shown. We were unable to compute the curve of SNLCs delineating the transition from e to g.

2.4.1.3 Basins of attraction

Given a circular trail sufficiently large that there is a stable fixed point, we first examine the dependence of the basin on the radius and the turning sensitivity, β in Fig. 9. In Fig. 9A, $r_0 = 1$ and $\beta = 1, 10$ while in 9B, $r_0 = 4$. For smaller radii, higher sensitivity does not necessarily mean that the basin will be bigger. Indeed, there are initial conditions that lie in the basin of attraction for $\beta = 1$ (red) , but not when $\beta = 10$ (blue). On the other hand for large radii (Fig. 9B), the basin for $\beta = 10$ contains that for $\beta = 1$.

Since there are no stable fixed points for spot location, we can consider the ability of an individual to orient toward a spot given that it is frozen ($v = 0$) at a distance, r, from the spot. In this case, we have a simple one-dimensional system:

$$\dot{\xi} = \beta\big[C_L(r, \xi) - C_R(r, \xi)\big]$$

with a stable fixed point at $\xi = \pi$. The eigenvalue around this fixed point is:

$$\lambda(r, l, \phi) = -\beta 4lr \sin(\phi) \exp(-r^2 - l^2 + 2lr\cos(\phi))$$

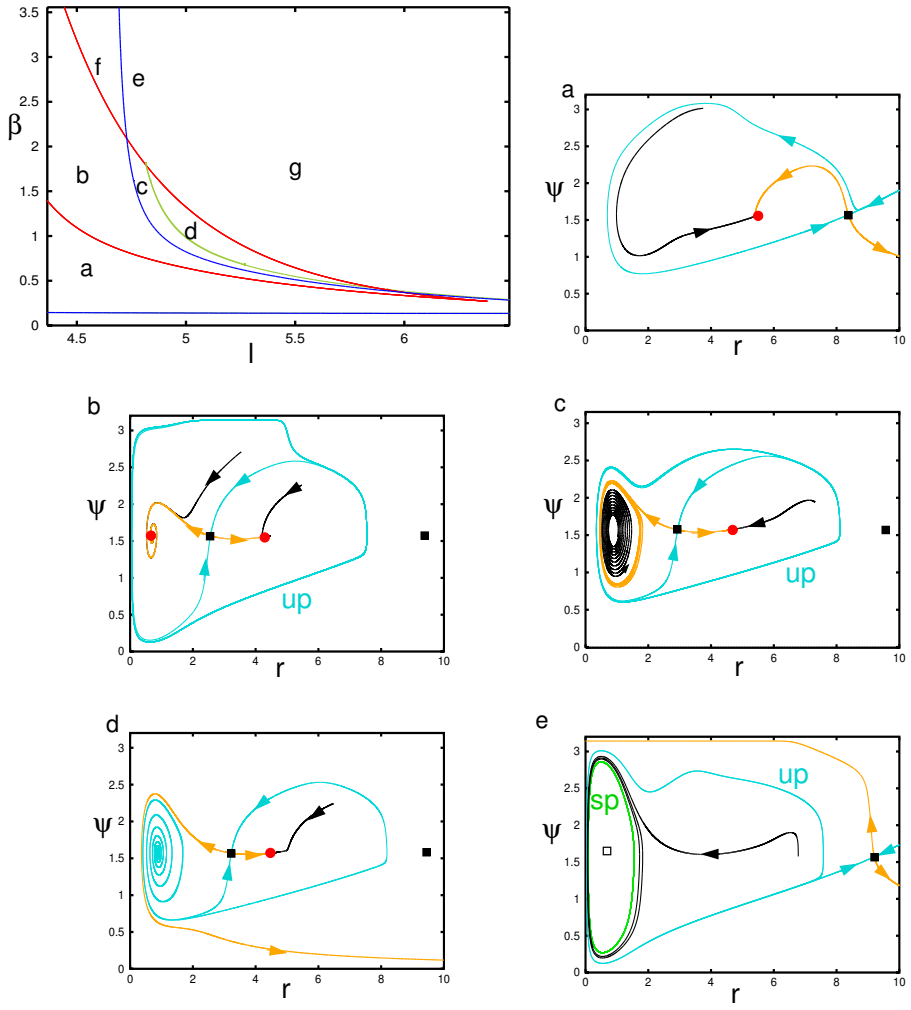

Figure 7: Dynamics on circular trail (here $r_0 = 4, \phi = 1$) when l is large and β is small. The dynamics is organized by the saddle-nodes or folds of equilibria (red), the Hopf bifurcation (blue), and a homoclinic bifurcation (olive). Phaseplanes in the representative regions are depicted. Stable (cyan) and unstable (orange) manifolds of the saddles (filled black squares) are shown along with some representative trajectories (black). Stable fixed points are red circles, saddles are black squares, unstable nodes are hollow squares. UP:unstable periodic orbit; SP:stable periodic orbit. Region f is like region e, but the stable periodic orbit is replaced by a stable fixed point. In region g, there are no attractors. Panel e shows a stable isolated limit cycle in green. More details in the text. Parameters (l, β): (a) (4.5,0.5), (b) (4.5,2), (c) (4.85,1.25), (d) (4.93,1.25), (e) (4.72,3)

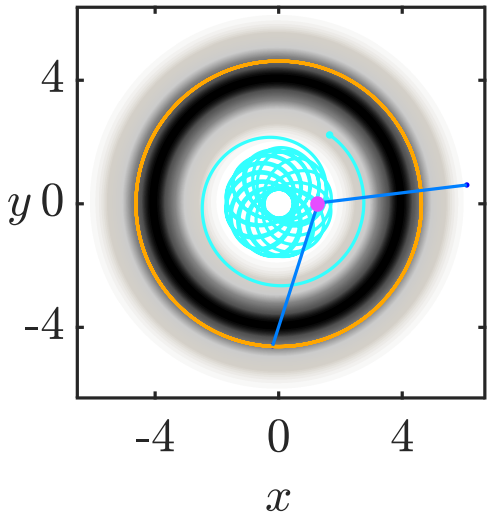

Figure 8: Projection of the trajectory of the individual in the (x, y, θ) model in region c of Fig. 7. Outer orange circle is a stable path of the individual, grayscale shows trail concentration. Stable torus solution shown in cyan. Magenta spot is the individual with the sensors drawn to scale in blue. Animation can be found in supplementary video.

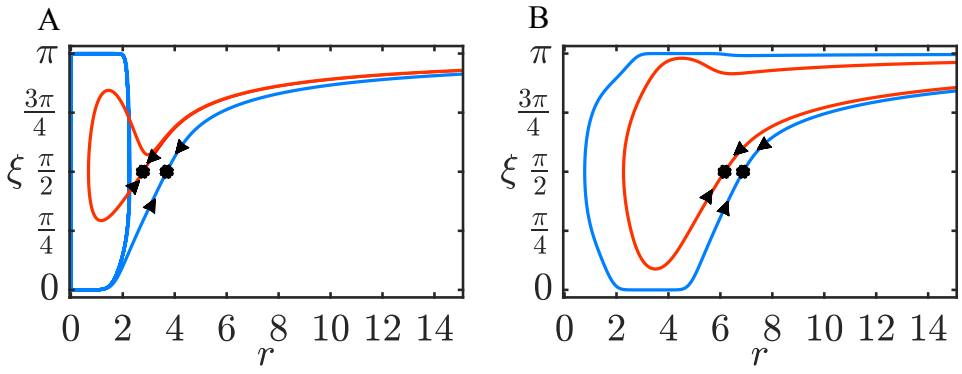

Figure 9: (A) Basin of attraction when trail is circular with radius $r_0 = 1$. (B) Basin of attraction when trail is circular with radius $r_0 = 4$. For both figures, blue and red lines correspond to the basin when $\beta = 10$ and $\beta = 1$ respectively.

and, as with the trail, this has a minimum at a particular value of ϕ:

$$\frac{d\lambda}{d\phi} = -4\beta lr\exp(-r^2 - l^2 + 2lr\cos(\phi))\big(\cos(\phi) - 2rl\sin^2\phi\big) = 0.$$

Solving for $\cos\phi$, we get

$$\cos\phi = \frac{-1 + \sqrt{16(rl)^2 + 1}}{4rl} := M.$$

As $rl \to 0$, $M \to 0$ and as $rl \to \infty$, $M \to 1$. In particular, this suggests that close to the spot (rl small), the animal should keep its sensors near $\pm\pi/2$ while keeping them close to 0 when it is far from the spot.

2.4.1.4 Integrability

As in the case of an infinite line, system (4) can be approximated by an integrable system for small l:

$$\begin{aligned} \dot{r} &= \cos\xi \\ \dot{\xi} &= [4l\beta\sin(\phi)(r - r_0)\exp(-(r - r_0)^2) - 1/r]\sin\xi, \end{aligned} \tag{5}$$

with

$$E := log(|\sin\xi|) + 2l\beta\sin(\phi)\exp(-(r - r_0)^2) + log(r) = \text{constant}.$$

We arrive at system (5) by looking at:

$$\lim_{l\to 0}\frac{C_L - C_R}{l} = \lim_{l\to 0}\frac{1}{l}\bigg[\exp -\big(r_L - r_0\big)^2 - \exp -\big(r_R - r_0\big)^2\bigg].$$

We will simplify $\frac{C_L}{l}$ first then use similar calculations for $\frac{C_R}{l}$.

$$\begin{aligned} \frac{C_L}{l} &= \frac{1}{l}\exp\Big(-\big(r_L - r_0\big)^2\Big) = \exp\Big(-r_L^2 - r_0^2 + 2r_L r_0\Big) \\ &= \frac{1}{l}\exp\Big(-r^2 - l^2 - 2rl\cos(\xi + \phi) - r_0^2 + 2r_0\sqrt{r^2 + l^2 + 2rl\cos(\xi + \phi)}\Big) \\ &= \frac{\exp(-r^2 - r_0^2)}{l}\exp(-l^2)\exp\Big(-2rl\cos(\xi + \phi) + 2r_0\sqrt{r^2 + l^2 + 2rl\cos(\xi + \phi)}\Big). \end{aligned}$$

Using Taylor's expansion,

$$\begin{aligned}
\frac{C_L}{l} &= \frac{\exp(-r^2-r_0^2)}{l}(1-l^2+l^4+\cdots)\Big(1-2rl\cos(\xi+\phi)+2r_0\sqrt{r^2+l^2+2rl\cos(\xi+\phi)} \\
&+ \frac{\big(-2rl\cos(\xi+\phi)+2r_0\sqrt{r^2+l^2+2rl\cos(\xi+\phi)}\big)^2}{2} \\
&+ \frac{\big(-2rl\cos(\xi+\phi)+2r_0\sqrt{r^2+l^2+2rl\cos(\xi+\phi)}\big)^3}{3!}+\cdots\Big) \\
&= \frac{\exp(-r^2-r_0^2)}{l}(1-l^2+l^4+\cdots)\Big(1-2rl\cos(\xi+\phi)+2r_0\sqrt{r^2+l^2+2rl\cos(\xi+\phi)} \\
&+ \frac{4r^2l^2\cos^2(\xi+\phi)+4r_0^2(r^2+l^2+2rl\cos(\xi+\phi))}{2} \\
&- \frac{8rr_0l\cos(\xi+\phi)\sqrt{r^2+l^2+2rl\cos(\xi+\phi)}}{2} \\
&+ \frac{-8r^3l^3\cos^3(\xi+\phi)+8r_0^3(r^2+l^2+2rl\cos(\xi+\phi))^{\frac{3}{2}}}{3!} \\
&+ \frac{24r^2r_0l^2\cos^2(\xi+\phi)\sqrt{r^2+l^2+2rl\cos(\xi+\phi)}}{3!} \\
&- \frac{24rr_0^2l\cos(\xi+\phi)(r^2+l^2+2rl\cos(\xi+\phi))}{3!}+\cdots\Big).
\end{aligned}$$

Similarly, we simplify $\frac{C_R}{l}$ to get

$$\begin{aligned}
\frac{C_R}{l} &= \frac{\exp(-r^2-r_0^2)}{l}(1-l^2+l^4+\cdots)\Big(1-2rl\cos(\xi-\phi)+2r_0\sqrt{r^2+l^2+2rl\cos(\xi-\phi)} \\
&+ \frac{4r^2l^2\cos^2(\xi-\phi)+4r_0^2(r^2+l^2+2rl\cos(\xi-\phi))}{2} \\
&- \frac{8rr_0l\cos(\xi-\phi)\sqrt{r^2+l^2+2rl\cos(\xi-\phi)}}{2} \\
&+ \frac{-8r^3l^3\cos^3(\xi-\phi)+8r_0^3(r^2+l^2+2rl\cos(\xi-\phi))^{\frac{3}{2}}}{3!} \\
&+ \frac{24r^2r_0l^2\cos^2(\xi-\phi)\sqrt{r^2+l^2+2rl\cos(\xi-\phi)}}{3!} \\
&- \frac{24rr_0^2l\cos(\xi-\phi)(r^2+l^2+2rl\cos(\xi-\phi))}{3!}+\cdots\Big).
\end{aligned}$$

Therefore, taking the limit of the difference between concentrations

$$\lim_{l\to 0}\frac{C_L-C_R}{l}=\lim_{l\to 0}\frac{\exp(-r^2-r_0^2)}{l}(1+\mathcal{O}(l^2))\Big[-2rl\Big(\cos(\xi+\phi)-\cos(\xi-\phi)\Big)$$
$$+2r_0\Big(\sqrt{r^2+l^2+2rl\cos(\xi+\phi)}-\sqrt{r^2+l^2+2rl\cos(\xi-\phi)}\Big)$$
$$+4rr_0^2l\Big(\cos(\xi+\phi)-\cos(\xi-\phi)\Big)$$
$$-4rr_0l\Big(\cos(\xi+\phi)\sqrt{r^2+l^2+2rl\cos(\xi+\phi)}-\cos(\xi-\phi)\sqrt{r^2+l^2+2rl\cos(\xi-\phi)}\Big)$$
$$+\frac{4}{3}r_0^3\Big((r^2+l^2+2rl\cos(\xi+\phi))^{\frac{3}{2}}-(r^2+l^2+2rl\cos(\xi-\phi))^{\frac{3}{2}}\Big)$$
$$-4rr_0^2l\Big(\cos(\xi+\phi)(r^2+l^2+2rl\cos(\xi+\phi))-\cos(\xi-\phi)(r^2+l^2+2rl\cos(\xi-\phi))\Big)$$
$$+\mathcal{O}(l^2)+\cdots\Big].$$

Simplifying, we get

$$\begin{aligned}\lim_{l\to 0}\frac{C_L-C_R}{l}&=\exp(-r^2-r_0^2)\Big[-2r(-2r\sin\xi\sin\phi)+\frac{2r_0 2r(-2\sin\xi\sin\phi)}{2r}\\&\quad+4rr_0^2(-2\sin\xi\sin\phi)-4rr_0(-2r\sin\xi\sin\phi)+\frac{4}{3}r_0^3\frac{3r^4 2r(-2\sin\xi\sin\phi)}{2r^3}\\&\quad-4rr_0^2(-2r^2\sin\xi\sin\phi)+\cdots\Big]\\&=\exp(-r^2-r_0^2)\Big[4r\sin\xi\sin\phi(1+2rr_0+\frac{(2rr_0)^2}{2!}+\cdots)\\&\qquad-4r_0\sin\xi\sin\phi(1+2rr_0+\frac{(2rr_0)^2}{2!}+\cdots)\Big]\\&=\exp(-r^2-r_0^2)4(r-r_0)\sin\xi\sin\phi\exp(2rr_0)\\&=4(r-r_0)\exp(-(r-r_0)^2)\sin\xi\sin\phi.\end{aligned}$$

For $K:=\beta l\sin(\phi)$ large enough, the integrable system has a saddle and a nonlinear center; the stable manifolds of the saddle form a good approximation for the basin of attraction for (4), even for $l=1$, over a wide range of the other parameters. This calculation does not say anything about the stability of the fixed point; rather, it gives some insight into the regions of attraction. Figure 10 shows that the even for $l=1$, the basins of the full equation (4) and the integrable system (5) are close.

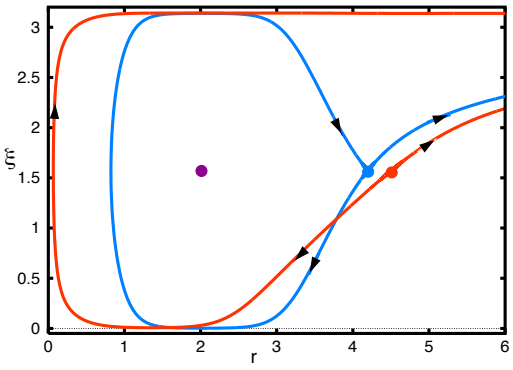

Figure 10: Comparison of the basin of attraction for the full model (4) (red) with that of the integrable approximation (5) (blue) for $l = 1, \beta = 4, r_0 = 2, \phi = 1$. Saddle points are shown in their respective colors. The stable fixed point and nonlinear center are nearly coincident and shown in purple.

As with the linear trail, radially symmetric odor gradients can also be reduced to planar dynamical systems. Nevertheless, they produce complex behavior including multi-stability and different types of stable and unstable limit cycles. Circular trails with a large enough radius lead to a stable movement clock-wise or counter-clockwise around the trail when the sensors are short. Such trajectories are seen in so-called ant-mills (where large populations of ants move in a circular trail until they die of exhaustion)[66]. Because the individual has a constant speed, it is not possible for the point source to be an attractor. However, the model does take the individual toward the source (depending on its initial distance and heading), so, in a real situation where the source is some reward the animal would stop moving when it reached the source.

2.5 Multiple sources

When an animal is searching for food, there can be multiple sources that affect the concentration detected and could be used to localize an odor source. We next study how the bilateral model behaves in the presence of two odor sources. With more than one source, the radial symmetry is broken and we cannot exploit the reduction in dimension used above. Thus, we will use the (x, y, θ) system and the concentration detected will be the sum of the Gaussian concentration of the spots.

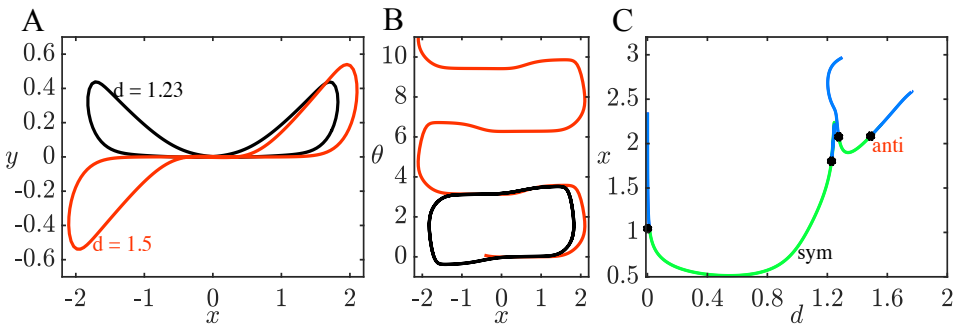

Figure 11: Two different types of trajectories for concentrations with two odor sources located on the x-axis a distance d apart, centered at $x = 0$. (A) Projection into the (x, y) plane; (B) Projection in the (x, θ) plane; (C) Bifurcation diagram for the two different cases in (A and B) as d varies. Other parameters are $\beta = 20, l = 0.5, \phi = 1$.

Without loss of generality, we place the *two* point sources at a distance d from each other on the x-axis and analyze the dynamics of Eq. (1). The odor concentration at the first spot is $C_1(x, y) = A_1 \exp\big(-\big((x + d/2)^2 + y^2\big)\big)$, and at the second spot is $C_2(x, y) = A_2 \exp\big(-\big((x - d/2)^2 + y^2\big)\big)$ where A_1 and A_2 are positive, possibly different, amplitudes. Thus, the concentration detected at the sensors is

$$C_L(x, y) = C_1(x_L, y_L) + C_2(x_L, y_L)$$
$$C_R(x, y) = C_1(x_R, y_R) + C_2(x_R, y_R),$$

$x_{L,R}, y_{L,R}$ are as in Fig. 1.

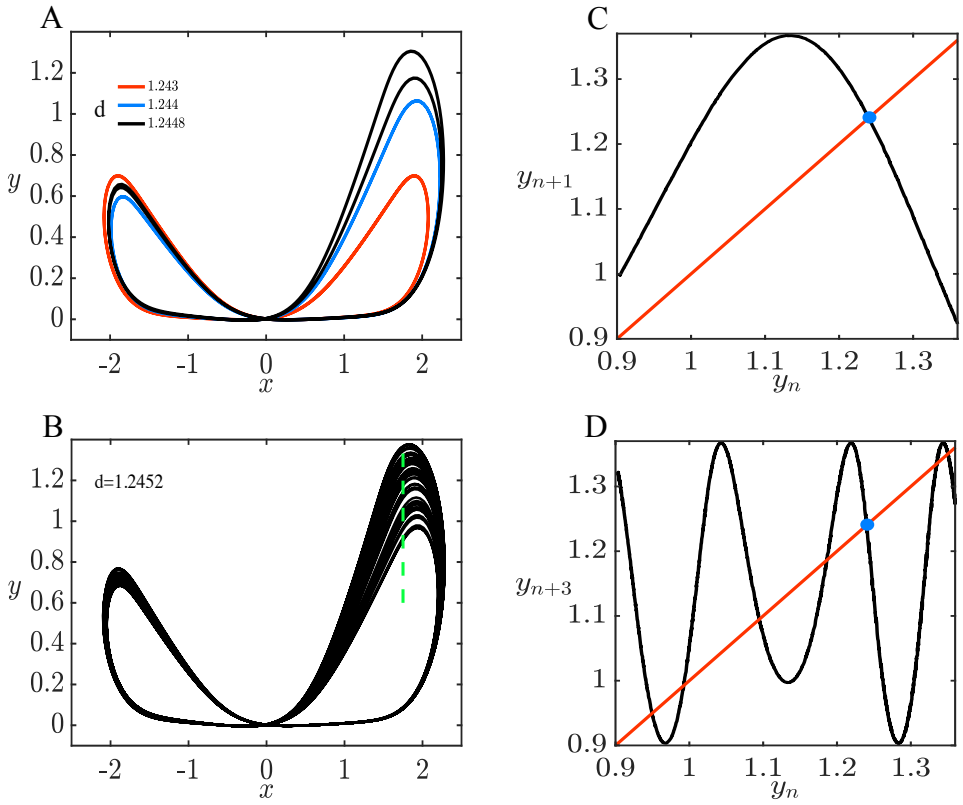

Figure 12: Behavior of Eq. (1) when there are two Gaussian sources at $(x, y) = (\pm d/2, 0)$. (A) As d increases, the symmetric periodic solution (red) loses stability and gives rise to a stable asymmetric solution (blue). Increasing d leads to a period doubled solution (black) which also loses stability as d increases. (B) Presumably chaotic behavior for $d = 1.2452$. (C) Poincare map through $x = 1.75$ for the solution in (B). Blue circle is unstable periodic orbit. (D) Same Poincare section showing the numerical existence of a period three orbit shown by the intersections of the $n+3$ iterate with the diagonal. The blue filled circle shows the period one fixed point. (Parameters are as in Fig. 11.)

Recall that in the case of a *circular trail*, there are stable fixed points in the polar form of the equations which correspond to circular periodic orbits in the (x, y, θ) system. Since the individual must maintain a constant speed, we cannot expect any fixed points in the (x, y, θ) system, so we will look for periodic orbits. We fix $\beta = 20, l = 0.5, \phi = 1$ in this section; the default values of β, l produce periodic orbits for a range of d, but the behavior is not as rich. In Figure 11A, we show two qualitatively different trajectories projected in the (x, y) plane for spots placed a distance d on the x-axis. At small values of d the trajectory is symmetric (black curve) and the heading, θ oscillates around $\pi/2$ (Fig. 11B, black) (topological winding number of 0). There is an analogous curve where $y(t) < 0$ and θ oscillates about $3\pi/2$. For a larger value of d, we find an anti-symmetric trajectory (Fig. 11A, red) and in this case, θ goes through all values with a net increase of 2π after each cycle (Fig. 11B, red) (topological winding number of 1). Fig. 11C shows the one-parameter bifurcation diagram as d changes for the symmetric and the anti-symmetric paths. The stability of these is lost at branch points marked by the filled blue circles. If we follow the symmetric branch point at the high value of d (close to 1.25), then a stable branch of asymmetric solutions emerges. This is shown in Fig. 12A as the blue curve. Increasing d along this asymmetric branch leads to a periodic doubling bifurcation (shown as the black curve). Further increases lead to presumably chaotic behavior, shown in Fig. 12B in the $(x, y)-$plane. To further quantify the chaos, we take a Poincare section through $x = 1.75$ and plot the points (y_n, θ_n) where x crosses from right to left. We find (not shown) that these points appear to lie along a one-dimensional curve, indicating that the underlying chaos can be understood by a one-dimensional map. Fig. 12C shows the map where we plot (y_n, y_{n+1}). It appears to be a typical cap map. The periodic orbit (blue circle) is unstable as the slope through it is less than -1. Fig. 12D shows (y_n, y_{n+3}) plotted and a clear period 3 orbit that is also unstable. Since the underlying dynamics seems to be governed by a one-dimensional map, we believe that Fig. 12B represents a truly chaotic orbit. Additionally, the maximal Liapunov exponent is 0.045, a positive number, yet another character of chaos.

As the previous figures show, if the spots are close to each other, there can exist solutions where the individual circles *both of them*. Furthermore, when there is an isolated spot, there are no stable bounded solutions as we saw above. However, the presence of a distant spot

(at least over a small range of distances) can stabilize periodic orbits around a spot. Fig. 13A shows two different stable trajectories around a source at $(-d/2, 0)$. The red solution is symmetric about the y-axis ($d = 2.5$) and the black solution has lost the symmetry ($d = 2.43$). This branch of periodic solutions exists for a narrow range of values of d as shown in the bifurcation diagram in Fig. 13B. In particular as d decreases, there is a supercritical pitchfork bifurcation that leads to the stable asymmetric solution shown in panel A. For d increasing,there is a subcritical pitchfork which together with the other pitchfork forms an isolated branch of asymmetric solutions.

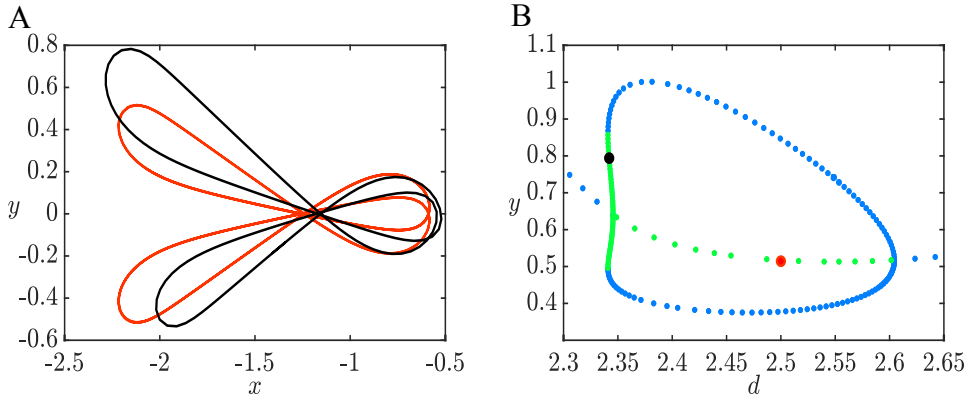

Figure 13: Two distant sources. (A) Stable periodic circling around the source at $(-d/2, 0)$ with the other source located at $(d/2, 0)$ with $d = 2.5$ (red) and $d = 2.34$ (black). (B) Bifurcation of the isolated periodic orbit as d changes. There are two pitchfork bifurcations whose branches form an isolated loop. Filled circles correspond to orbits depicted in A. Remaining parameters as in Fig. 11

Another interesting question is how the behavior changes when the concentrations at the spots are different in magnitude. Fig 14A shows trajectories when the amplitudes of the spot are equal and the spots are at a relatively large distance from each other (such that there is no periodic orbit encircling them). Depending on the initial position, trajectories either pass through both spots, just one of the spots or miss them both. In all cases, however, the trajectories diverge. This is also true when we increase the amplitude of one of the spots by 5-fold as in Fig 14B. Note that the individual spends some time wandering around the spot with higher intensity before wandering off. On the other hand, when we bring the

spots closer to each other as well as increase the amplitude (Fig 14C), the trajectories that go to the spot with larger amplitude will oscillate around this spot. Thus, the existence of the weaker spot at a distance can stabilize the trajectory around the spot with a higher concentration, just as we saw in Fig. 13. The periodic solution shown in Fig. 14C persists for much larger values of A_2 and will also persist for A_2 reduced to 1, where the resulting periodic solution is the same as that seen in Fig. 13A (red).

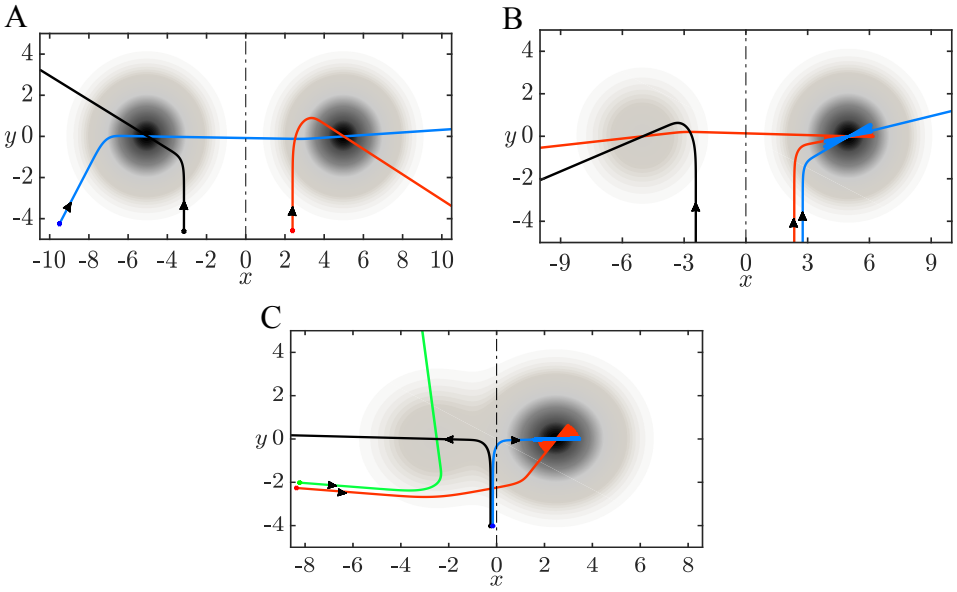

Figure 14: Different trajectories when: (A) Both sources have the same amplitude ($A_1 = A_2 = 1$) and are at a distance ($d = 10$) where the 2 sources are distinguishable. (B) Second source has significantly larger amplitude ($A_2 = 5$). (C) Second source has significantly larger amplitude and the sources are closer to each other ($d = 5$) Other parameters as in Fig. 11.

More complex dynamics can occur with three or more sources. In this case, however, there are many different possible configurations thus we will not consider them further.

2.6 Finite Trails

We have looked at how the bilateral model performs when we have an infinite line and circular trails. Now we will examine its behavior on a finite line segment and a finite line

segment with gaps, sharp angles and branches, as these cases can be tested in animal behavior experiments.

If we start close enough to a segment trail, the model will find the trail, follow it and then leave it. When β or l is small, trajectories will have damped oscillations that decay slower as we decrease β or l (Fig 15). The starting angle affects the trajectory orientation; most trajectories continue to the right when θ_0 is less than $\frac{\pi}{2}$ and to the left when θ_0 is larger than $\frac{\pi}{2}$. Similarly, if we start around the gap, then we take either the left or right branch depending on the starting position and angle. Also, we can find the trail from significantly farther distances when we start around the gap which is also the case when we start around the beginning or end of the trail. An individual will cross the gap and reacquire the trail when the gap is in a line trail that has no angles or turns. This is true because once the trail is acquired in the bilateral model, the individual will keep moving straight on it. However, if either β or l is small, and the oscillations are large near the gap, the model will sometimes lose the trail as in Fig 15B.

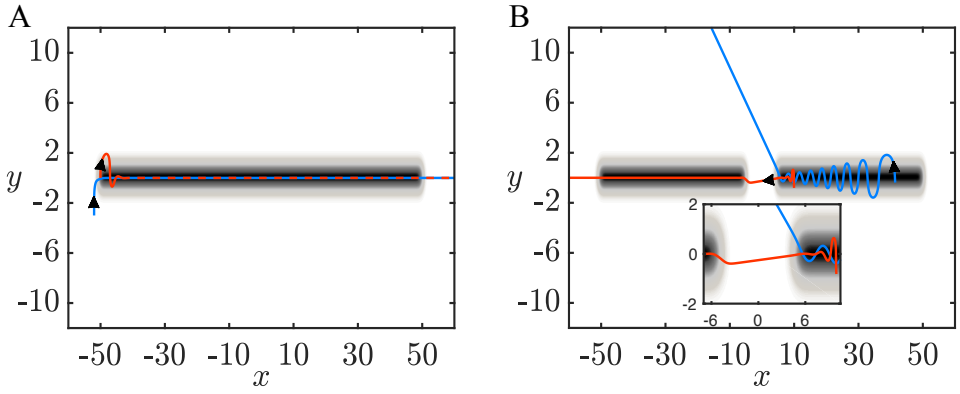

Figure 15: (A) Trajectories on a segment trail. Red line is when β is 5 fold smaller than the blue line trajectory. (B) Trajectories can either cross gaps or lose the trail depending on β or length of nares l. Red trajectory is when $l = 0.4$ and Blue trajectory is when $l = 0.1$.

If there is an angle in the trail, then it must be larger than $\frac{\pi}{4}$ for the model to follow it easily. In Fig 16A, the model is able to correct and follow the trail when the angle is slightly bigger than $\frac{\pi}{4}$, but as soon as the corner angle is $\frac{\pi}{4}$, the model loses the trail.

When the trail bifurcates into two branches, the angle and amplitude of each branch

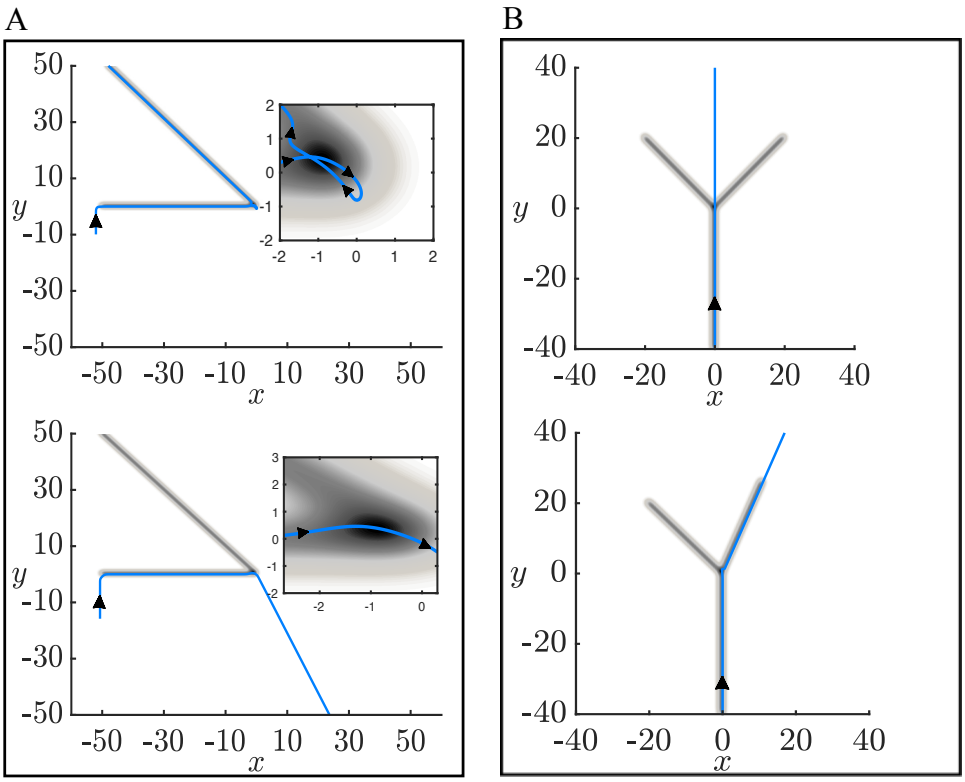

Figure 16: A. (top) Trail with angle very close but greater than $\frac{\pi}{4}$. Zoomed on how model is able to correct and find trail. (bottom) Trail with angle equal to $\frac{\pi}{4}$. Zoomed on how model can not sense the change in the angle and loses trail. B. (top) Y trail, the branches are at equal angles from the main trail. (bottom) Y trail where the branches are at different angle from the main trail. The blue line is a trajectory starting at the main trail.

determine the trajectories of the model as it passes the branch. We observe that when an individual starts on the main trail that has two branches at equal angle and amplitude (top panel of Fig 16B), it will continue on a straight path as there is no difference in the left and right concentrations due to symmetry. However, if the symmetry is broken, say, the branch angles are unequal, (bottom panel of Fig 16B), then the individual will go towards the branch that requires the least amount of turning. This might not be the case if the concentrations on the two branches differ as the model will always turn toward the higher of the two concentrations at the sensors.

Trails with gaps and finite trails are similar to an infinite trail over the period of time in which the individual is on the segment. since once the individual finds the trail, it stays on it. If the trail is short and σ is large, then, there is behavior like two close spots, e.g. Fig. 11, otherwise, the individual eventually reaches the end of the trail and moves away. Thus, in these cases, there are no attractors and basins, bifurcations, etc do not make sense. We have included the results on branched and finite trails mainly because they provide for the possibility of experimentally testing some of the results. Indeed, some preliminary experiments in the lab of Nathan Urban examine the paths of mice that are trained to follow trails when the trails branch and have gaps.

2.7 Discussion

In this chapter, we analyzed a simplified dimensionless model that describes the use of bilateral information to navigate odor sources. We looked at how the model behaves in the presence of one or more odor spot sources, circular and infinite straight trails, and trails with gaps and angles. To allow for mathematical analysis of the model, some simplifications were applied. Instead of using more realistic odor description such as turbulent plumes [18], we present concentration as fixed Gaussian distributions. We also keep the function that determines the change in the heading angle linear in the difference between left and right concentration unlike previous work [12, 13]. Calenbuhr et. al [12, 13] put the concentrations through a Michaelis-Menten type nonlinearity so that saturation occurs at large

concentrations. These nonlinearities will not change the qualitative behavior (in fact, on an infinite trail, the fixed points are the same), but will alter some of the details like the basin of attraction and the degree of multistability. Some animals change their velocities while searching for odor sources (for example ants [25] and mice [45] decrease their velocity closer to the source), here though, we do not take variable velocity into consideration. With our simplifications, we are able to examine how the performance changes as we vary different parameters. The main parameters we look at in our scaled model are the length l of the sensors, the angle ϕ between the sensors and the sensitivity β to concentration change.

In the case of the infinite line, as we increase β, both the analytical and simulated basins of attraction increase which is expected since the change in heading angle becomes more sensitive to the concentration difference. When ϕ is larger or l is smaller, we see increased sinusoidal motion centered at the trail. When the odor source is a spot, one of the fixed points of the model is a saddle point and the other is unstable (at r close to 0). This suggests that the individual will not be able to find spot sources, however, we can see from figures (in (x, y) plane) that trajectories pass through the spot. The reason that the model moves away from the spot is that we have required that the speed stay constant. When multiple spot odor sources are added, the (x, y, θ) system exhibits trajectories that pass through one source or multiple sources, periodic orbits around sources and chaotic behavior. Because Gaussian circular trails share the radially symmetric property with single spots, we use the same (r, ξ) system to study how varying l, β and ϕ affects its stability and basin of attraction on these trails. The fixed point (circular trail) becomes stable at a small radius ($r_0 \sim 0.5$) and remains stable for all larger radii. As in infinite trails, when we increase β on a circular trail with large enough radius, the basin of attraction increases. This is not true for smaller radii or when we increase the length of the nares l where an optimal length $l < r_0$ gives the largest basin of attraction. When the odor source is a finite straight trail, the individual will keep on the trail once it finds it even if there is a gap because of the symmetry between the nares. If the trajectory is sinusoidal (e.g. Fig. 15B) then the individual can lose the trail at the gap depending on the amplitude of the fluctuations. When there is a trail with an angle, the individual turns and keeps on the trail if the angle is larger than $\pi/4$ and loses the trail

otherwise. If the trail bifurcates into two branches, we see that the individual chooses the branch with a smoother turn angle. This is seen in rats [41] where they tended to choose the branch that had a smaller angle with the main trail (straighter).

At a fixed sensor length l, there is an angle ϕ that makes the system most stable and have an optimal basin of attraction when the odor landscape is an infinite line. For a spot source, we are also able to find an optimal ϕ by freezing the individual while orienting it towards the spot ($\xi = \pi$) and studying the linearization of the new system. We conclude that the individual will best reach the source if it keeps ϕ closer to zero when it is away from the spot and closer to $\pi/2$ (large sinusoidal behavior) when it is near the spot. This contradicts the best strategy we found to acquire and stay on an infinite trail where it is better to have a smaller ϕ closer to the trail. This shows that animals consider different ways to optimize their search depending on the odor distribution. For example, similar to our results, in Draft et al [25], ants move their antennas to have smaller angles while following the trail and bigger angles when exhibiting sinusoidal movements near the trail. In Khan et al [41], rats were able to cross gaps and reacquire the trail by increasing the amplitude of their head casting (which might suggest that they are using the strategy discussed to best find infinite trails by changing their method since they can not control angle between nares). Also in Liu et al [45], mice exhibit an increase in sinusoidal behavior near the spot source and their trajectories become more tortuous.

Real odor landscapes are not simple smooth gradients, but, rather, temporally complicated and turbulent. In Boie et al [7, 25], the authors showed that the spatial information provided by the two sensors is non-redundant in turbulent plumes. We have tested the simple bilateral algorithm in a plume (not shown here) and we observe that the individual can successfully find the odor source. Similar to our previous results, we have to start at a position orienting towards the plume in order to find it because we do not add noise or a corrective method to turn the individual back once it veers off the plume. One major aspect that we have not explored in this chapter is the effects of noise on the models. There are several ways we could introduce this variability in the model. For example, the odor

concentration at a point in space could be converted to a rate for a Poisson process and the number of hits in some window of time could act as the main signal. In other work ([45]), we have used this type of model to mimic the behavior of mice looking for spots of odor. Another type of stochasticity that could be included is additive noise to the equation for θ. That is, in absence of any odor cue, the individual undergoes a correlated random walk. Such behavior is commonly seen as a foraging strategy for animals and in the present case would have the effect of allowing the individual to correct for starting conditions that, in the deterministic case, would lead it away from the odor source. Whether there is an optimal amount of such "noise" to maximize the probability of success is currently a subject of further research. The bilateral model explains many results observed in animal data but not all behavior. Understanding the underlying dynamics of the bilateral model will help in building models that use bilateral information together with other strategies such as casting or upwind orientation.

3.0 Effect of Adding Noise to Bilateral Olfactory Search and Navigation

3.1 Abstract

Animals use olfactory cues while navigating their environments to find food, locate mates and avoid danger. Previously, we studied the dynamics of the bilateral model, a strategy that depends on the simultaneous comparison between odor concentrations detected by left and right sensors. We showed that the agent has to be in a basin of attraction around the odor source in order to navigate towards the point source or follow the trail, else it fails. Thus, to improve the probability of finding the odor source, we employ a search strategy by adding noise to the heading angle in the bilateral model. We find that constant noise will be more successful when paired with a nonlinearity applied either to the concentration detected by the left and right sensors or to the difference in concentrations. We also show that concentration dependent noise improves performance on the spot source.

3.2 Introduction

In Chapter two, we looked at a deterministic bilateral model and provided a mathematical analysis to understand how bilateral information, on its own, can drive navigation. In this chapter, we will look at the effect of noise when added to the same model and how to interpret this noise in terms of navigation. In the previous chapter, we find that the agent has to be around the odor source in order to navigate towards the point source or follow the trail. However, from the behavior of animals, whether in experimental setting or naturalistic (open field) arenas, we notice that animals can still find odor sources and acquire trails even if their initial starting position is not close to the source. This indicates that even though animals depend on sensory cues to extract directional information, in the absence of a reliable sensory signal they use different strategies to first search for odorants and then to navigate them.

For an algorithm, that tries to find an existing or a suspected target, to be called a search strategy, there should be an uncertainty in either the sources or in how to find these sources (i.e. no cues should be driving the movement) [4]. There are two types of searches, systematic searches compared to random searches. systematic searches depend on a deterministic algorithms and some knowledge of the landscape [35] while random searches depend on stochastic processes. Random search strategies that have been proposed to characterize animal movements use either random walks or Levy walks. A random walk moves an agent some distance where it orients towards a random direction and then repeats the same action. Though simple to implement, random walks may result in redundant trajectories [10] and do not always describe realistic animal movement. The advantage of correlated random walks and Levy walks is that they result in less redundant paths and better describe animal behavior. These models allow for directional persistence of the movement, which is observed in animals, because the turning angles are not independent.

Two other distinctions affect a search strategy which are the availability of resources and the scale of the environments where the animals are searching. Many studies have suggested that in environments where the resources are abundant, models that allow for spending more time at a patch should be used such as correlated random walks. While in environments with scarce cues, models that optimize the animal's time and energy are more appropriate such as Levy walks. This brings up a trade-off between exploration of new possibilities and exploitation of already detected opportunities. This is sometimes referred to as intensive versus extensive search or even local versus global search [32, 22, 14].

In this chapter, we will examine how adding a stochastic term to the heading angle is going to affect the search efficiency of our model. In our setup, we fix the borders of the arena which restricts the search area and eliminates the need for a more extensive or spread search. Therefore, we want to switch from an exploratory to an exploitation strategy in a fixed space where the agent exists. This means that maximizing the search or area coverage is not an important factor in defining the search efficiency. Instead, we look to the number of times the animal is able to find the target while starting from anywhere in the fixed arena. Thus, we will quantify the efficiency as the probability of success in finding the odor source.

3.2.1 The Model

In all of the following sections, we will add noise to the heading angle θ of the bilateral model we analyzed before. For all the simulations, the odor concentration landscape is Gaussian with $\sigma = 2$, the length of the sensors is $l = 1$, the angle between the sensors is $\phi = 1$, the velocity is $v = 1$, and the measure of sensitivity to the concentration difference is $\beta = 10$ unless mentioned otherwise.

$$\begin{aligned} dx &= v\cos\theta dt \\ dy &= v\sin\theta dt \\ d\theta &= \beta\big[C_L - C_R\big]dt + kdW. \end{aligned} \tag{6}$$

3.3 Spot Source

3.3.1 Constant Noise

We first look at the effect of adding a constant noise to the heading angle θ in the model. This translates to adding a constant noise to the angle ξ in the reduced (r, ξ) system that we used in our previous work when the concentration landscape presented to the model is radially symmetric.

$$\begin{aligned} dr &= v\cos\xi dt \\ d\xi &= \beta\big[C_L - C_R\big]dt - \frac{v}{r}\sin\xi dt + kdW. \end{aligned} \tag{7}$$

For every noise value, we start at a random position in the domain with a random heading angle and check if the model is able to find the spot source successfully within the allotted time. We repeat this for $N = 50000$ simulations. Successful simulations occur when the trajectories cross a minimum value of r, r_{min}, while unsuccessful simulations occur when trajectories cross a maximum value of r set at r_{max} or run out of time before crossing r_{min}. Here we choose $r_{min} = 1$, since the source is at $r = 0$, and $r_{max} = 10$. Probability of success is

then calculated by dividing the number of successful runs by the total number of simulations N at every noise level, and mean time to source is calculated by adding the time it takes for every successful simulation to find the source and then dividing it by N.

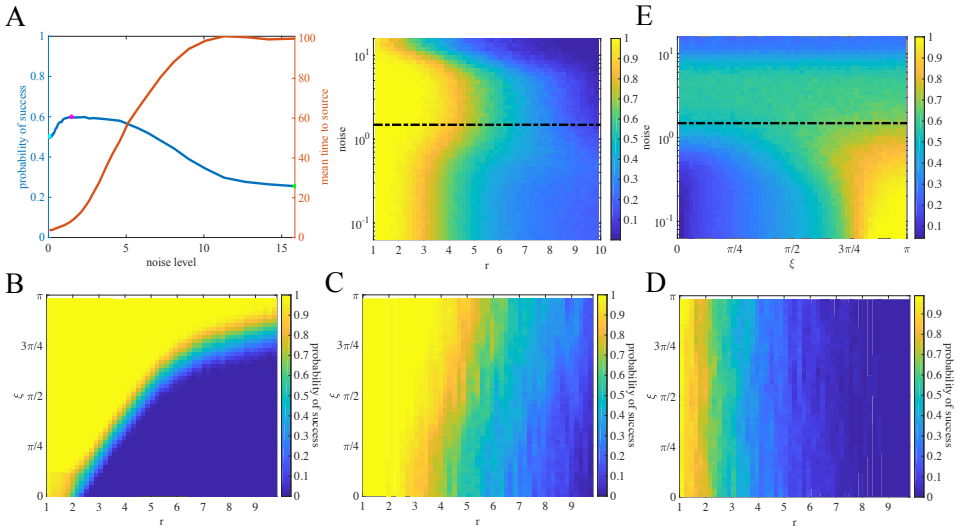

Figure 17: Probability of success as constant noise varies for a spot source. (A) Probability of success (blue) and mean time to source (red) as noise varies. (B,C,D) Distribution of the initial positions and the color changes according to probability of success. (B) At small noise = 0.063 (cyan in (A)), the probability of success is 0.5. (C) At optima noise = 1.484 (magenta in (A)), the probability of success is 0.6. (D) At large noise = 15.85 (green in (A)), the probability of success is 0.255. (E) Marginal Probabilities $P(r)$ (left panel) and $P(\xi)$ (right panel) where the noise axis is log scaled and the dashed black line is the optimal noise level.

From Fig. 17, we can see that the mean time to source increases with noise magnitude (which will be true for all the following figures) and there is an optimal noise level at 1.48 that gives the highest value of the probability of success at 60%. For small noise values, trajectories must start closer to the source to find it and since these trajectories do not have fluctuations, it takes them less time even though probability of success is not optimal. As the noise values increase, trajectories will have much more fluctuations and therefore it will take them longer to find the source. Fig. 17 also shows the distribution of the initial conditions across the domain and whether the agent is successful when starting from that

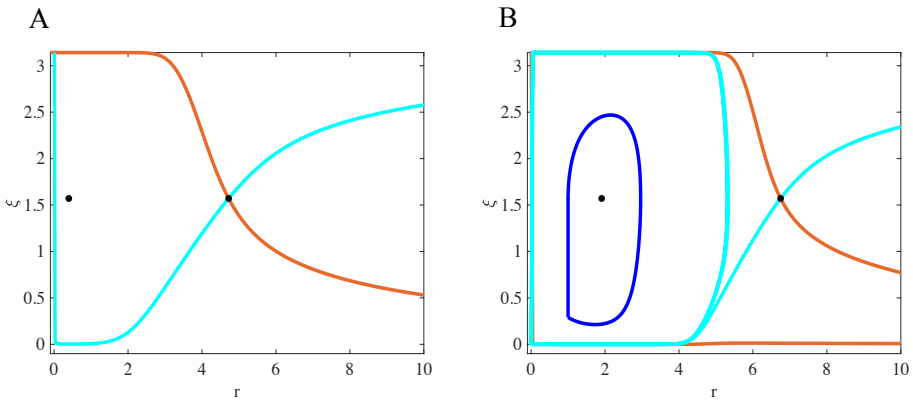

Figure 18: (A) Phaseplane of $(r, \xi)-$ system for a spot source has an unstable fixed point at $(0.398, \frac{\pi}{2})$ and a saddle point at $(4.72, \frac{\pi}{2})$ with the unstable manifold in orange and the stable manifold in cyan. (B) Phaseplane of $(r, \xi)-$ system for a spot source when a Hill function is applied. It has a stable fixed point at $(1.91, \frac{\pi}{2})$ and a saddle point at $(6.75, \frac{\pi}{2})$ with the unstable manifold in orange and the stable manifold in cyan. The blue curve is an invariant set.

initial condition. When the noise value is small at 0.06 in Fig. 17A, there is a boundary that separates the trajectories that find the source (in yellow) and those that do not (in blue). This boundary resembles the stable manifold that we see in the deterministic case (Fig. 18A). However, once more noise is introduced into the system, this boundary is broken and there is more variation in the probability of success. Now, the agent is no longer 100% successful when it is radially oriented toward the spot (ξ is close to π) and far away from the source. Instead, the boundaries become more vertical and the probability of success depends more on the distance to the source. When the noise is optimal at 1.48, the initial conditions in Fig. 17C can be grouped into different regions. When $r < 2$(yellow), the probability of success is 100% which then drops to $80 - 90\%$ for $2 < r < 4$, $60 - 80\%$ for $4 < r < 6$, and the probability gradually decreases to reach 0% for $r > 9$. When the noise is very large (Fig. 17D), we see that the region with success probability greater than 80% shrinks down to $r < 2$ and a clear region where the probability is zero emerges for $r > 6$.

3.3.2 Constant Noise with Non-linearity

3.3.2.1 Hill Function

Olfactory neuron receptors bind to odorants and the biophysics of this process results in a saturating relationship between the fraction of receptors closed and odor concentration [28, 52]. The Hill function which describes this saturating relationship has been shown to play a role in olfactory navigation [76]. Therefore, here, we will still add a constant noise to the heading angle θ in the (x, y, θ) system i.e. ξ in the reduced (r, ξ). However, now the first term of the heading angle will change to become the difference between nonlinear left and right concentrations.

$$\begin{aligned} dr &= v\cos\xi dt \\ d\xi &= \beta\big[\frac{C_L}{C_L + c_{min}} - \frac{C_R}{C_R + c_{min}}\big]dt - \frac{v}{r}\sin\xi + kdW. \end{aligned} \tag{8}$$

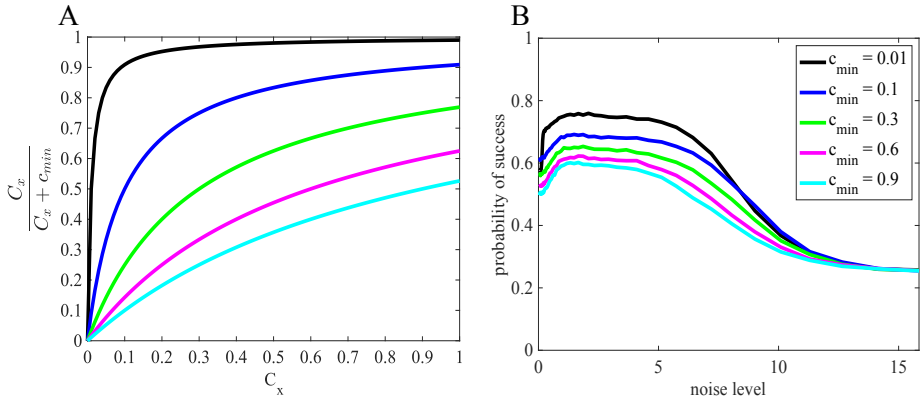

Figure 19: Effect of the sharpness of Hill function on the probability of success. (A) Odor Concentration detected for different c_{min} in Hill function. (B) Probability of success as noise varies for different c_{min}.

We vary c_{min} from eq. 8 in order to choose the best sharpness of the Hill function. Notice from Fig. 19A that as c_{min} get smaller, $\frac{C_x}{C_x + c_{min}}$ becomes more sensitive to lower concentration values. Therefore, when $c_{min} = 0.01$, the Hill function amplifies very low concentration values and saturates to 1 much faster than when all the other values of c_{min}

are used. Fig. 19B shows that the smaller values of c_{min} also improve the probability of success which is the reason why we choose $c_{min} = 0.01$ to continue our analysis.

From Fig. 20A, we observe that the probability of success starts at 57.5% for small noise values, then an optimal noise level at 2 maximizes the probability at 76% where it plateaus for a range of noise values and falls off to 25% for very large noise. For small noise at 0.06, Fig. 20B exhibits two boundaries that separate initial conditions that are successful in finding the source (in yellow) from unsuccessful trajectories (in blue). The outside boundary resembles the stable manifold in the deterministic case. To understand the inside boundary which shows trajectories that start near r_{min} but are unsuccessful in reaching the source, we look at the effect of adding a Hill function on the phase plane. In Fig. 18B, we observe that there is a change in the fixed points coordinates and stability when a Hill non-linearity is introduced to the deterministic system. The two fixed points are shifted to larger values of r where the first fixed point at $r \approx 1.91$ becomes stable and the second fixed point remains a saddle. Therefore, trajectories starting around the stable fixed point will be attracted to it instead of trying to reach $r = 0$ where the source is. We find an invariant set (blue curve in Fig. 18B) such that trajectories starting within will converge to the fixed point without crossing $r_{min} = 1$ and trajectories starting outside of this set will hit $r_{min} = 1$ and come close to the source while they spiral towards the fixed point. The inside boundary that we get in Fig. 20B corresponds to this invariant set. As more noise is added, trajectories will fluctuate and will not be contained in this invariant set, thus crossing $r_{min} = 1$ which will cause the inside boundary to disappear. The outside boundary changes since the initial conditions with coordinates between $2 < \xi < \pi$ and $8 < r < 10$ which were successful at low noise levels because they were radially oriented towards the spot are no longer 100% successful. The probability of success now will fall off as the agent moves away from the source. We detect this clearly in Fig. 20C where the success is maximized and in Fig. 20D where the probability is at its minimum for large noise. Fig. 20C shows that the probability of success is 100% for $r < 5$ and gradually drops as the agent starts farther away from the source. Similarly, Fig. 20D shows the probability of success is high for $r < 2$ then decreases to reach zero for all trajectories starting at $r > 6$.

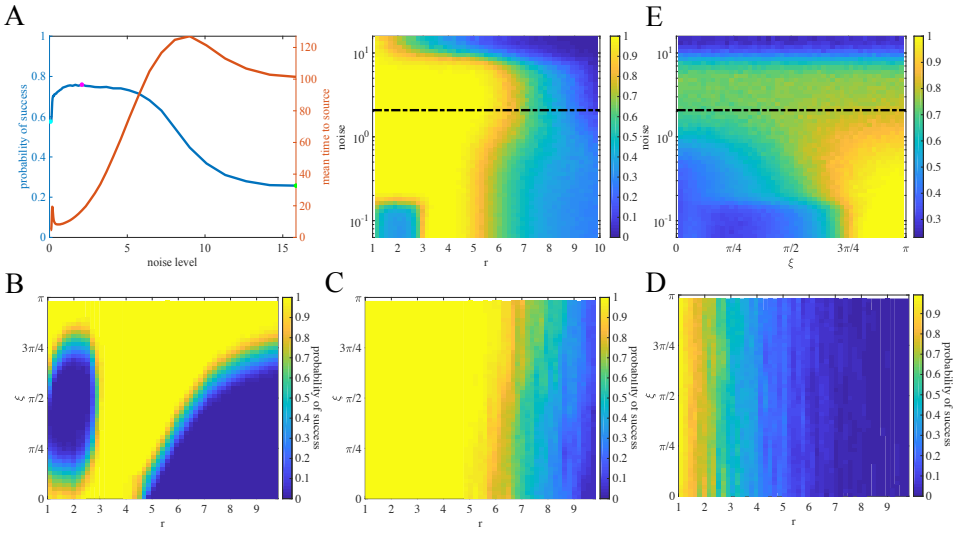

Figure 20: Probability of success of model with Hill function applied to C_L and C_R as constant noise varies. (A) Probability of success (blue) and mean time to source (red) as noise varies. (B,C,D) Distribution of the initial positions and the color changes according to probability of success. (B) At small noise = 0.063 (cyan in (A)), the probability of success is 0.575. (C) At optimal noise = 2.08 (magenta in (A)), the probability of success is 0.76. (D) At large noise = 15.85 (green in (A)), the probability of success is 0.257. (E) Marginal Probabilities $P(r)$ (left panel) and $P(\xi)$ (right panel) where the noise axis is log scaled and the dashed black line is the optimal noise level.

3.3.2.2 Tanh

Instead of applying a Hill function to the left concentration and right concentration, we apply a tanh non-linearity to the difference between the concentrations. We start with $\tanh(10(C_L - C_R))$ and we increase the sharpness until we reach $\tanh(100(C_L - C_R))$. In the deterministic case, we still have two fixed points with one of them being a saddle. We observe that the basin of attraction created by the stable manifold of the saddle point increases as we increase the sharpness of tanh. Here, we do not see the invariant set that shows up in the Hill function case. The increase in the basin of attraction can be seen in Fig. 21 where the cyan colored points represent the probability of success for low noise which increases from 62% to 70% as the sharpness of tanh increases from 10 to 100. The maximum probability of success also increases from 70% to 76% with the sharpness of tanh. The probability of success curve is similar to Fig. 20A when a Hill function is applied where we observe a plateau before the probability drops for very large noise values.

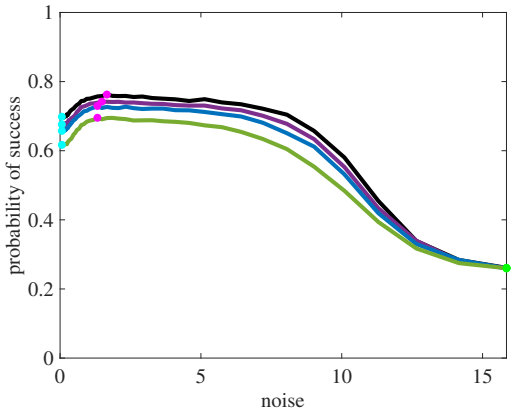

Figure 21: Effect of the sharpness of tanh on the probability of success. The green curve is $\tanh(10(C_L - C_R))$, the blue curve is $\tanh(30(C_L - C_R))$, the purple curve is $\tanh(50(C_L - C_R))$ and the black curve is $\tanh(100(C_L - C_R))$.

3.3.3 Concentration Dependent Noise

We now know that adding constant noise to the bilateral model improves the probability of finding the source. From the phase plane of the $(r, \xi)-$ system, we observe that the plane is divided into two regions, the first region is above the stable manifold where trajectories starting there will cross the source and the second region which is below the stable manifold such that trajectories starting there will veer off and not come across the source. Intuitively, we think that adding a constant level of noise at every position might not the best strategy. If the agent is in the second region where trajectories usually veer off, then adding a high noise term might be helpful to find the source but large noise values might push the agent away from the source if it is in the first region. Therefore, we introduce a noise term that is concentration dependent such that lower noise values are required when the concentration detected is high and the agent is at a closer proximity to the source and higher noise values are used when the odor concentration is low or not detected at all. The noise is again added to ξ in the reduced $(r, \xi)-$ system and contains two parameters that affect its value, α which affects the magnitude of the noise and γ that affects the slope of the noise as a function of the average of the concentration detected by the left and right sensors.

$$\begin{aligned} dr &= v\cos\xi dt \\ d\xi &= \beta\big[C_L - C_R\big]dt - \frac{v}{r}\sin\xi dt + +\alpha\exp\big(-\gamma\frac{C_L + C_R}{2}\big)dW. \end{aligned} \tag{9}$$

We start by investigating the best γ to choose which will then describe how the noise is changing with odor concentration. To do this, we set α to 2 and then examine the change of the probability of success as we vary γ. Here we find that the probability keeps on increasing as we increase the value of γ as shown in Fig. 22A. This suggests that the best strategy is a fast switching mechanism where noise is turned off or set to very low values once any odor concentration is detected. So we choose an appropriate value for γ (we choose $\gamma = 100$) and then vary α to address the effect of changing the magnitude of this noise type. Similar to the case of constant noise, we again find that there is a value of α that maximizes the probability of success. At small values of α (Fig. 23B), we see the same boundary that separates

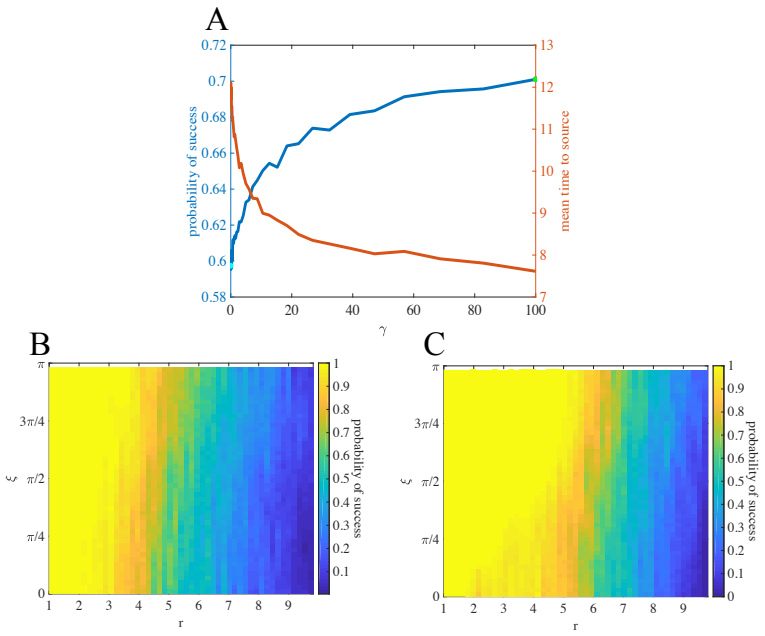

Figure 22: Probability of success as the slope of the concentration dependent noise is varied. (A) Probability of success (blue) and mean time to source (red) as γ varies when the amplitude of the noise is set to $\alpha = 2$. (B) When $\gamma = 0.01$, mean time to source = 12.11 and probability of success = 0.59 which corresponds to smallest noise. (C) When $\gamma = 100$, mean time to source = 7.6 and probability of success = 0.7 which corresponds to optimal noise (green in (A)) .

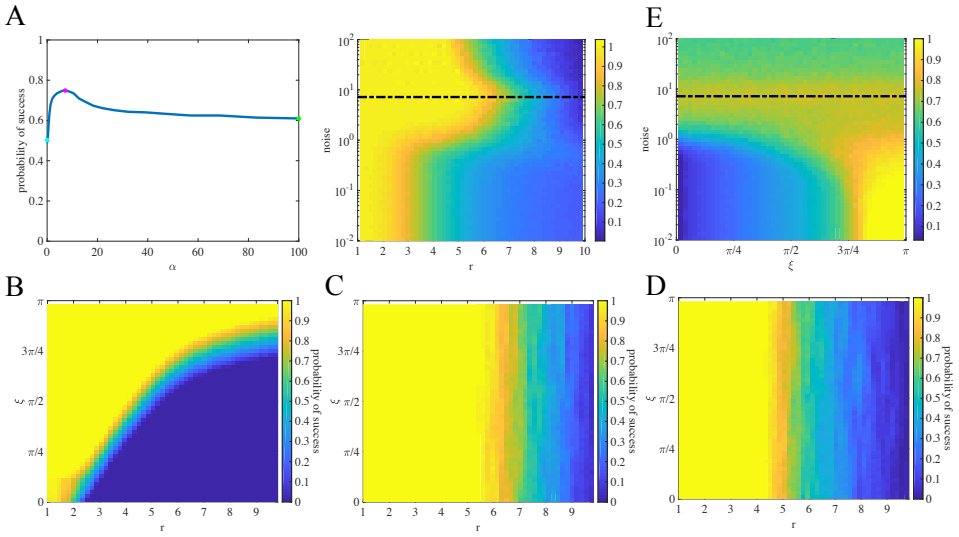

Figure 23: (A) Probability of success as α varies when $\gamma = 100$. (B,C,D) Distribution of the initial positions and the color changes according to probability of success. (B) At small noise magnitude $\alpha = 0.01$ (cyan in (A)), the probability of success is 0.5. (C) At optimal noise magnitude $\alpha = 7.2$ (magenta in (A)), the probability of success is 0.75. (D) At large noise magnitude $\alpha = 100$ (green in (A)), the probability of success is 0.61. (E) Marginal Probabilities $P(r)$ (left panel) and $P(\xi)$ (right panel) where the noise axis is log scaled and the dashed black line is the optimal noise level.

successful from unsuccessful starting points. Then at $\alpha = 7.2$, the probability of success is the highest at 75% and we observe in Fig. 23C that the domain is divided into 5 regions. In the first region, $r < 6$, the agent is always successful. Then the probability of success drops to $80 - 90\%$ when the agent starts in $6 < r < 7$, it drops further to $60 - 70\%$ in the region $7 < r < 8$, it becomes around 50% in $8 < r < 9$ and then zeroes out in the region where $r > 9$.

From Fig. 23A and 23D, we observe that at higher values of α, the probability of success plateaus at around 60% which comes as a surprise since one would expect a much lower probability akin to the results we get for high values of constant noise (Fig. 17D and Fig. 20D). To understand what is going on at large α values, we first check whether this is an effect of the high value of γ. We observe from Fig. 24 that the probability of success persists at higher values than we expected for larger noise magnitude for all the different slopes γ of the concentration dependent noise. We conclude that this result then is not a byproduct of the chosen slope. We next investigate whether this is due to averaging. Therefore, in Fig. 25A, we again choose $\gamma = 100$ and fix r at different values in our domain instead of choosing both initial conditions r and ξ randomly. Here we notice that for $r = 1.5$, $r = 2.5$ and $r = 3.5$, the probability of success remains $= 1$ for all the magnitudes α of noise. We begin to see a change in the probability once $r = 4.5$ (purple curve), but the main decrease in the probability for larger α occurs when $r = 5.5$ (green curve). Thus, as long as r is less than 4.5, the probability remains high and for $r \geq 7.5$, the probability becomes small for large α. To explain the reason behind these r numbers, we look at the noise ($= \exp(-100C(r))$) as a function of r. From Fig. 25B, we find that for $r < 3$, the noise is always zero because the odor concentration detected is higher than the threshold that would turn the noise switch on. Hence, for these values of r where the agent is close to the source, the magnitude α will not affect the 100% probability of success since the noise is already zero here. A very small noise (< 0.15) is then introduced for $3 < r < 4$ which then increases rapidly when no concentration is detected to become ≈ 1 for r greater than 6. Now, the high magnitudes of the noise will tremendously worsen the probability of success and we get the plateau once we average all the curves for different r (black dashed curve in Fig. 25A).

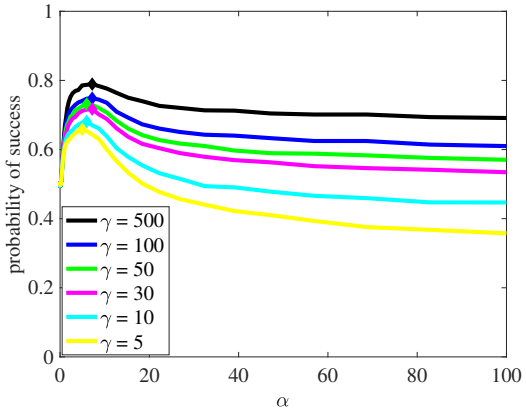

Figure 24: The probability of success for different values of γ.

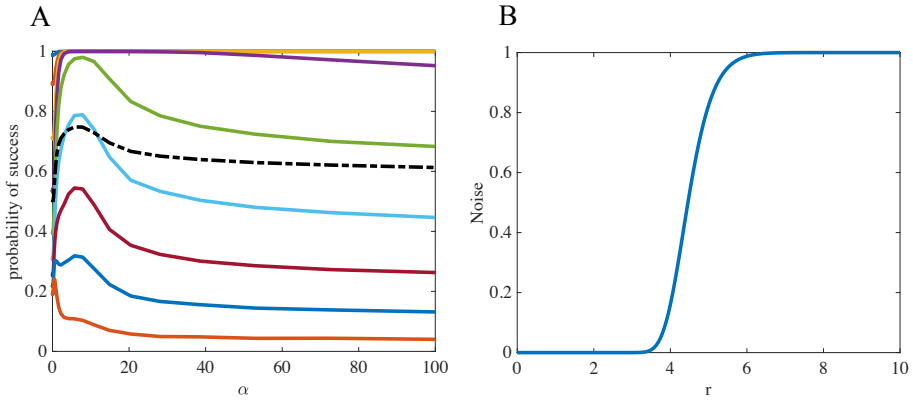

Figure 25: (A) Probability of success as α varies when we start at a fixed value r and a random value ξ, $noise = \alpha \exp(-\gamma \frac{C_L + C_R}{2})$. The topmost curve in dark blue corresponds to $r = 1.5$, the red orange curve for $r = 2.5$, the yellow curve for $r = 3.5$, the purple curve for $r = 4.5$, the green curve for $r = 5.5$, the light blue curve for $r = 6.5$, the red curve for $r = 7.5$, the blue curve which is second from bottom corresponds to $r = 8.5$, and the last orange curve for $r = 9.5$. The black dashed curve is the average. (B) $noise = \exp(-100C(r))$ as a function of r.

Next, we add a non-linearity, either by applying a $\tanh(100(C_L - C_R))$ or a Hill function to both C_L and C_R, and check whether using a concentration dependent noise will improve on the results we get when adding constant noise. We find that when tanh is used, the probability of success starts at 76% and fluctuates around this value as γ varies. Though the mean time to source decreases as γ increases which is similar to the result we get when the difference between the left and right odor concentrations are linear, we do not find a similar trend for the probability of success as in Fig. 22A. Therefore, if we consider the probability of success as the only measure of efficiency, then constant noise is enough to improve when tanh is applied. If, however, we were to consider the mean time to source as our efficiency measure, it might then be useful to examine adding concentration dependent noise further. When we apply a Hill function with $c_{min} = 0.01$ to both C_L and C_R, we find that the probability of success peaks at very small value of $\gamma = 0.017$ and decreases as γ increases. This shows that the best noise to add when we are using a Hill function is the constant noise that gives the optimal success probability in Fig. 20C.

3.4 Infinite Line

3.4.1 Constant Noise

In this section, we will again add a constant noise to the heading angle θ in the system (x, y, θ). This system is planar when we the odor landscape is an infinite line along the $y-$ axis.

$$dx = v\cos\theta dt \tag{10}$$

$$d\theta = \beta\big[C_L - C_R\big]dt + kdW. \tag{11}$$

This model has two stable fixed points at $(0, \pm\frac{\pi}{2})$ which correspond to going up or down the line. In the previous chapter, we show that there is a basin of attraction around the

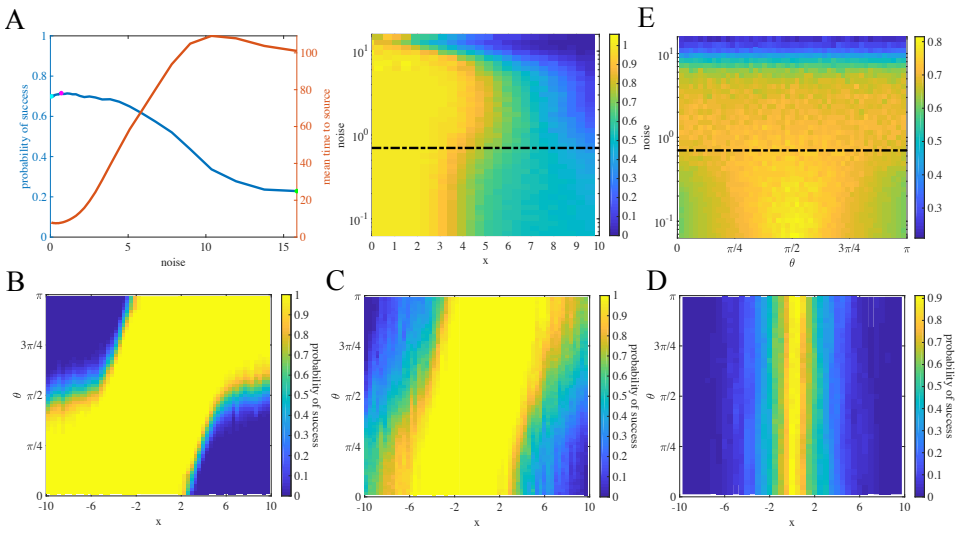

Figure 26: Probability of success as constant noise is varied for an infinite line. (A) Probability of success (blue) and mean time to source (red) as we change the constant level of noise. (B,C,D) show the distribution of initial conditions and color changing according to probability of success. (B) At small noise = 0.063 (cyan in (A)), the mean time to source is 7.95 and probability of success is 0.699. (C) At optimal noise = 0.7 (magenta in (A)), the mean time to source is 7.85 and probability of success is 0.715. (D) At large noise = 15.85 (green in (A)), the mean time to source is 101 and probability of success is 0.23. (E) Marginal Probabilities $P(r)$ (left panel) and $P(\xi)$ (right panel) where the noise axis is log scaled and the dashed black line is the optimal noise level.

stable fixed point even though the model does not exhibit a saddle point. As long as the trajectories start within this basin, the agent will find and follow the trail, else it might cross the line but it will not follow it. Because this basin of attraction exists, we want to examine if we can start somewhere outside this region and still find and follow the trail. We start by adding a constant noise to θ and exploring its effect on the behavior of our model. The agent is successful in following the trail if it comes very close to the trail ($-1 < x < 1$) and has crossed the trail at least twice. We enforce the second condition in order to ensure that an instance where the agent crosses the trail but keeps on moving away from it is not counted as a hit. To count a run as a failure, we study two cases. In the first case, we start from a specific domain and we consider it a failure once trajectories leave this domain. In the second case, we allow for trajectories to leave the domain we start from and the agent fails if it does not follow the trail within the allocated time. Probability of success and mean time to source are then calculated in the same manner as in the spot source.

In the following infinite line simulations, we used 50,000 simulations where $l = 1$, $\phi = 1$, $v = 1$, $\beta = 10$ and the concentration is Gaussian with $\sigma = 2$. Fig. 26 shows the probability of success, mean time to source and distribution of initial conditions when trajectories are not allowed to cross the domain. The domain here is $-10 \leq x \leq 10$, and we find that the probability of success does not improve significantly when noise is added. When the noise is very small, the probability of success is around 70% and it increases to a maximum of 71.5% when noise is optimal. There is a plateau around this value for some range of noise and then the probability starts decreasing to reach 23%. The mean time to source increases as we increase noise levels and it takes the shortest time to the trail when the noise is the lowest. If we look at the distribution of initial conditions, we find that in Fig. 26B when the noise is small, 0.06, the boundaries of the initial conditions from which trajectories acquired the trail corresponds the basin of attraction in the deterministic case in Fig. 29 (blue curve). In Fig. 26C, when the noise at 0.7 gives the maximum success, the inside of what resembles the basin still follow the trail 100% of the time. However, adding noise breaks the symmetry of the model. Thus, the part of the basin where the agent starts far from the trail but continues towards it just because the initial heading is directed towards

the trail no longer has a 100% success probability but rather the probability decreases as we move farther from the trail to reach around 60%. Similarly, in the regions that never find the trail in Fig. 26B (blue) because the agent starts heading away from the trail and can not detect any concentration that will help in correcting its turn, will in Fig. 26C succeed $20-60\%$ in following the trail depending on the distance to the trail. Adding noise aids the agent to turn without detecting concentration which will then put the agent in a higher concentration gradient that will allow it to acquire the trail. For very large noise levels, we see from Fig. 26D that noise will be very detrimental to the agent performance which will only find the trail if it is in a concentration gradient.

In Fig. 27, we inspect the effect of allowing trajectories to leave the domain they start in. Here, all parameters and the domain size are the same as in Fig. 26, and the only difference is counting failures as trajectories that do not follow the trail within the allotted time. We can directly see the improvement in the probability of success in Fig. 27A. The probability starts around 74%, peaks at 92% and then falls off quickly as the noise increases to reach 23% for very high noise. Fig. 27B shows that, for small noise, the distribution of initial conditions that lead to successful runs is almost the same as in Fig. 26B. The same goes for the case of very high level of noise where Fig. 27D and Fig. 26D are very similar. The major difference occurs when the noise is optimal at 0.75 which gives the best probability of success. The region where the the probability is 100% grows a little bit larger than what it is in Fig. 26C and wherever the agent starts outside of the yellow region, it is $70-90\%$ successful in following the trail. From Fig. 27C, we see that the lowest probability calculated is 60% which occurs at the most difficult positions to follow the line: on the edge of the domain facing away from the trail.

3.4.2 Constant Noise with Hill function

In this section, we check whether applying a non-linearity to the concentration will improve the performance of the model when the odor landscape is an infinite line as it does when the odor is a spot source. Here, we apply a Hill function to C_L and C_R and a steep

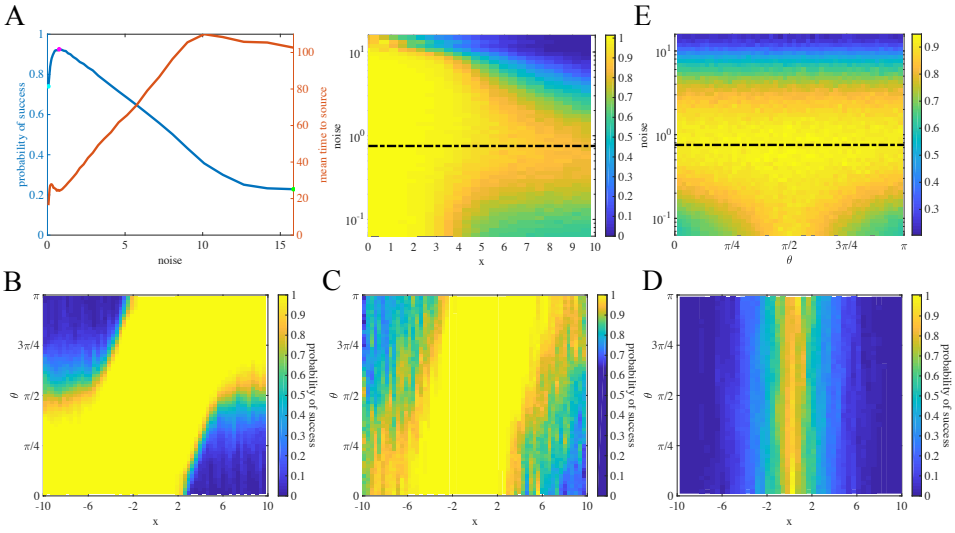

Figure 27: Probability of success when trajectories can cross domain as constant noise is varied for an infinite line. (A) Probability of success (blue) and mean time to source (red) as the constant level of noise changes. (B,C,D) show the distribution of initial conditions and color changes according to probability of success. (B) At small noise = 0.063 (cyan in (A)), the mean time to source is 16.4 and probability of success is 0.74. (C) At optimal noise = 0.754 (magenta in (A)), the mean time to source is 24.24 and probability of success is 0.925. Here, the smallest probability of success is 0.6. (D) At large noise = 15.85 (green in (A)), the mean time to source is 102.65 and probability of success is 0.23. (E) Marginal Probabilities $P(r)$ (left panel) and $P(\xi)$ (right panel) where the noise axis is log scaled and the dashed black line is the optimal noise level.

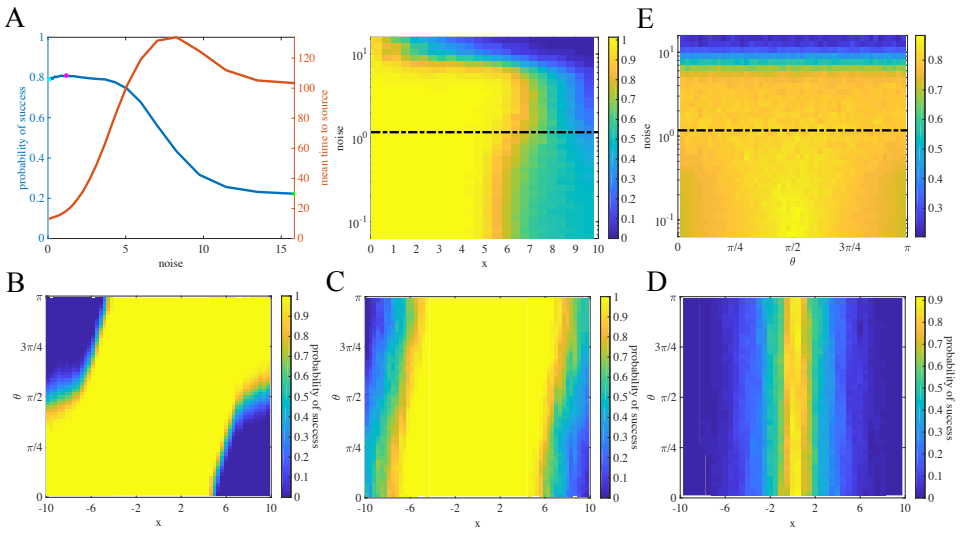

Figure 28: Probability of success when Hill function is applied as constant noise is varied. (A) Probability of success (in blue) and mean time to source (in red) as we the constant level of noise varies. (B,C,D) show the distribution of initial conditions and color changing according to probability of success. (B) At small noise = 0.063 (cyan in (A)), the mean time to source is 13.24 and probability of success is 0.79. (C) At optimal noise = 1.17 (magenta in (A)), the mean time to source is 18.39 and probability of success is 0.81. (D) At large noise = 15.85 (green in (A)), the mean time to source is 103.37 and probability of success is 0.22 . (E) Marginal Probabilities $P(r)$ (left panel) and $P(\xi)$ (right panel) where the noise axis is log scaled and the dashed black line is the optimal noise level.

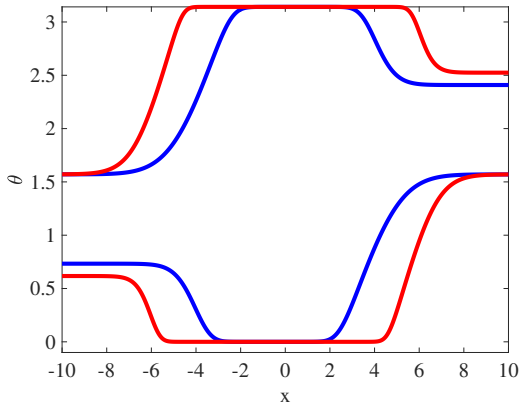

Figure 29: The blue curves are the basin of attraction when the change in θ depends on the linear difference between the concentration detected on the left and right sensors. The red curves are the basin of attraction when a Hill function is applied to C_L and C_R.

tanh to the difference in the concentrations. We had very similar results for both so we will only show figures for the Hill function.

Fig. 28A shows the probability of success and mean time to source as constant noise varies. Here, it is considered a failure if trajectories cross the boundaries. We get very similar results to when the concentrations detected are not amplified (Fig. 26A). It is important to note that what differs is the probability of success at small noise levels which in Fig. 26A is 70% but becomes approximately 80% when a Hill function is used. Fig. 29 explains this increase because once a Hill function is applied, the basin of attraction expands (red curves). This can also be seen in Fig. 28B in which the boundary between successful and unsuccessful runs resemble the basin of attraction in the deterministic case. However, though we see little change between the probability of success at low noise compared to the optimal noise, the distribution of the initial conditions that allow for successful runs changes such that the probability of success becomes more dependent on distance from trail.

When we allow the trajectories to cross the boundaries of the domain, noise at 0.84 will produce a maximum probability of success at 96% in Fig. 30A instead of it being 82% in Fig.

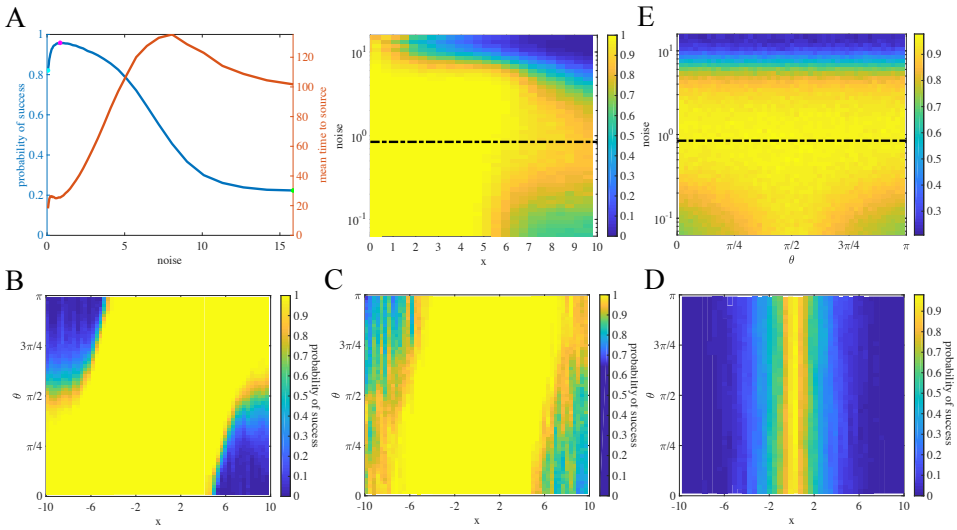

Figure 30: Probability of success when Hill function is applied and trajectories can cross domain. (A) Probability of success (blue) and mean time to source (red) as we change the constant level of noise. (B,C,D) show the distribution of initial conditions and color changing according to probability of success. (B) At small noise = 0.063 (cyan in (A)), the mean time to source is 18.2 and probability of success is 0.82. (C) At optimal noise = 0.844 (magenta in (A)), the mean time to source is 25.5 and probability of success is 0.96. Here, the smallest probability of success is around 0.6. (D) At large noise = 15.85 (green in (A)), the mean time to source is 101.75 and probability of success is 0.22. (E) Marginal Probabilities $P(r)$ (left panel) and $P(\xi)$ (right panel) where the noise axis is log scaled and the dashed black line is the optimal noise level.

28. This is a big improvement and can be seen in Fig. 30C where there is a high probability to acquire the trail no matter which positions the agent starts from. At very small and high noise levels, we have the same results as in Fig. 28.

We then examine if this trend continues when the domain size is larger. We expect that the model will still exhibit an optimal noise level which maximizes success rate but the probability will peak at a lower value than before. In Fig. 31, we choose the domain to be $-20 < x < 20$ and the results are exactly what we predict. The probability starts at 68% and peaks at around 85% which is lower than what we get in Fig. 30A then it decreases to 11% when the noise is very high. From Fig. 31C, we observe that the agent is at least 60% successful in acquiring the trail even when it starts very far away from the trail except at the edges of the domain where the probability drops to 50%.

3.5 Probability of Exiting the Arena at the Source

There are other measures to assess the performance or efficiency of the strategies we used. One such measure is to look at the probability of exiting the arena at the source. For a spot source, if the system is initially at some position r at time t, we ask what is the probability that at a future time s it will exit the arena through r_{min}. This probability $P(r, \xi))$ is similar to the idea of probability of success. It satisfies $P(r_{min}, \xi)) = 1$, $P(r_{max}, \xi)) = 0$, $P(r, \xi + 2\pi) = P(r, \xi)$. $P(r, \xi))$ and is described by :

$$0 = f(r, \xi)\frac{\partial P}{\partial \xi} + D_1\frac{\partial^2 P}{\partial \xi^2} + v\cos(\xi)\frac{\partial P}{\partial r} + D_2\frac{\partial^2 P}{\partial r^2}$$

where $D_1 = \frac{k^2}{2}$, k is the noise level used in Monte Carlo simulations, and $f(r, \xi) = \beta(C_L - C_R) - \frac{v}{r}\sin\xi$. We used a finite element method software to solve the partial differential equation. We get similar results to the figures in first section above especially for small enough diffusion levels. However, we find that even if only constant noise is added, at large diffusion levels, the probability of success plateaus at unexpected high values. Similar results are observed with concentration dependent noise. We are not sure the exact reason behind this and whether it is a byproduct of averaging.

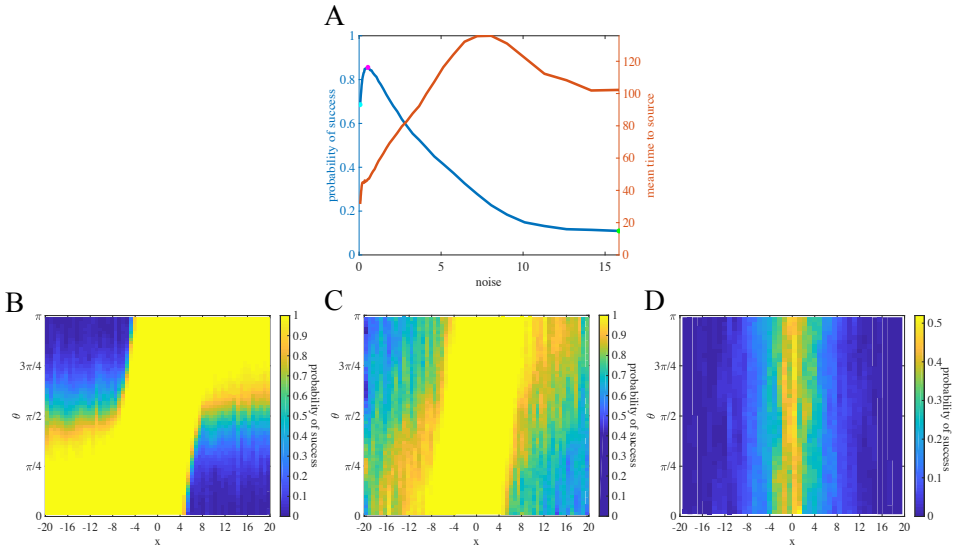

Figure 31: Probability of success when Hill function is applied and trajectories can cross a bigger domain. (A) Probability of success (blue) and mean time to source (red) as we change the constant level of noise. (B,C,D) show the distribution of initial conditions and color changing according to probability of success. (B) At small noise = 0.063 (cyan in (A)), the mean time to source is 31.6 and probability of success is 0.685. (C) At optimal noise = 0.54 (magenta in (A)), the mean time to source is 46.93 and probability of success is 0.855. Here, the smallest probability of success is around 0.5. (D) At large noise = 15.85 (green in (A)), the mean time to source is 102.25 and probability of success is 0.11.

3.6 Discussion

In this chapter, we examined the effect of adding noise to the bilateral model when the odor landscape is a Gaussian spot source or an infinite line. We used constant noise and concentration dependent noise and then calculated the probability of success to measure the performance of each strategy. We also looked at how the model behaves in the presence of noise when a non-linearity, whether a Hill function or tanh, is applied to the odor concentration. We find that there is an optimal level of noise that makes it beneficial to the system. This is an example of stochastic resonance [51, 48] which has been observed in many biological systems and in foraging [21, 27, 30, 63]. This noise could be external noise, sensory noise or even noise in the motor system. Here, the noise we added makes the turning angle more random than when only bilateral information is used.

In the case of a spot source, constant noise on its own improves the performance of the bilateral model. However, the performance is greatly enhanced when a Hill function or tanh is applied to the concentration. In the deterministic case, tanh does not affect the stability of the fixed points exhibited by the original system. The Hill function, on the other hand, changes the first unstable fixed point to a stable fixed point causing some trajectories close by to converge to it without crossing the source. That is the reason why, for small noise, the model with tanh outperforms that with the Hill function. Once an optimal level of noise is added, both models with non-linear functions have similar performance which surpass the model with a linear function of concentrations. This coincides with results showing the importance of a Hill function in olfactory navigation strategies [76] which governs the response of olfactory receptors [52, 28].

When the odor is an infinite line, the basin of attraction in the deterministic case increases when a non-linearity is applied. We only showed figures for the Hill function, but this is also true when a steep tanh is used. Thus, the probability of success is larger when the low concentrations are amplified. With or without a non-linearity, the probability of success peaks at an optimal noise level and then decreases for larger noise values. A very

small noise (< 1) is needed to maximize the probability of success at a value $> 90\%$. This shows that bilateral information is really helpful when the task is to follow trails. Moreover, if only a small noise is added to the model, the agent will be able to move more, with some tortuosity, that allows it to turn without detecting concentration in order to get out of no odor regions to sample odor at other regions.

One thing that we were able to find for the spot source but not for the infinite line was the effect of using concentration dependent noise. When we tried adding it for the infinite trail, we did not observe anything significant. This was also the case for the spot source when we added concentration dependent noise to the models with non-linear functions of concentration. However, when the model did not have a Hill or tanh function, concentration dependent noise greatly increased the performance. Therefore, we find that the best noise to add to the bilateral model (when its has a linear function of concentration difference) is the concentration dependent noise that switches off abruptly once a very small odor concentration is detected. We can think of this as a transition from a global search where a correlated random walk is used to move around the environment into a local search where only the difference between concentrations detected on the sensors is used. We call this a local search because once concentration is detected then we are close to the odor source due to the use of Gaussian distribution to describe the target. This abrupt transition which has been observed in animals such as C-elagans [14] and mice [45] was measured experimentally by the turning rate and velocity change. Calhoun et al. [14] used a drift diffusion model fitted to parameters of infotaxis trajectories to describe this transition that they found to be maximally informative. Our results here depend only on instantaneous detection of the concentration without any memory measure that tracks odorant hits and no hits (evidence accumulation).

It has been shown that animals [25, 45] tend to decrease their velocities when they get closer to odor sources. Liu et al. [45] also showed that removing concentration dependent velocity while modeling mice behavior, during a spot source localization task in a closed arena, severely decreased the performance of the model. In our model, we increased the con-

stant velocity and used a concentration dependent velocity such that the agent slows down next to the source. Increasing the velocity was helpful on the infinite line when trajectories could leave the domain especially when the domain size was expanded. We saw no effect of using a concentration dependent velocity over constant velocity. However, on the spot and on trails where trajectories failed if they hit the boundary of the domain, both velocity types worsened the success rate. This might be due to not allowing trajectories to leave the domain or bounce off the boundaries. Also, concentration dependent velocity might be more useful if the heading angle depended on temporal sampling and not just the spatial sampling that we have in our model.

Adding multiplicative noise to the concentrations detected by the sensors did not affect the probability of success. In future work, We would like to further explore concentration noise as well as investigate whether adding colored noise might be helpful to the model. Also, we want to test how noise affect the behavior and performance of the model on more realistic plumes.

4.0 Mouse Navigation on Bifurcated Odor Trails

4.1 Introduction

Studies of animals following scent trails have been previously conducted on ants [55, 25], rodents [37, 41, 77, 49], dogs [71, 36], moles [15, 16] and humans [57]. These studies have shown that animals use stereo olfaction to navigate, however, if one of the antennae or nostrils is blocked, animals are still able to follow odor sources though their accuracy and performance decrease and their trajectories become more tortuous. During navigation, animals also tend to have lateral back-and-forth behavior. These back-and-forth movements or casting are seen as evidence of active sampling of the odor [3]. However, this zigzagging increases in amplitude either when the odor signal is lost (rats in [41]), one of the sensors detecting concentration is lost (moles with stitched nostrils in [15]) or when mice get closer to odor point sources where the concentration becomes higher instead of lower [45]. Therefore, how this sampling of odor concentration is employed by animals and how they modulate its magnitude to track trails or localize sources are still unclear.

Tracking is a complex problem especially in naturalistic arenas where trails are affected by different factors [36] causing the odor signal to be intermittently detected. Still, the odor landscape is more stable and fluctuates less than odor plumes especially during lab experiments because the odor is near surface [18]. The experiments studied here are conducted in low wind conditions which is likely to preserve the spatiotemporal information of the odor trails near the surface.

In this chapter, we analyze trajectories of mice following odor trails and try to find behavioral patterns that can be associated with the use of either bilateral or inter-sniff information. We will simulate a model utilizing bilateral information with noise and check whether this will be enough to follow the trails. We will further investigate the role of casting in future work.

4.2 Methods

4.2.1 Behavioral Arena

The following experiments were done by Annie Liu in Nathan Urban's lab. A behavioral arena that was designed before and described in details in Jones and Urban, 2018 ([37]) was used to collect the trails data. It measures 36×45 inches which is held above the ground by an aluminum frame. Infrared IR light-emitting diodes (LEDs) were used to illuminate the arena to allow the camera (1280×1024 resolution, 11.2 pixels/cm, 50 frames/s, Flea3, Point Gray Imaging) which was fixed below the arena to record the mice behavior in the dark. All other light sources were handled so that mice can not rely on visual cues to complete the trials [37, 45].

4.2.2 Training

Mice were on food restriction to motivate them to engage in the task. While training the mice, they were placed in the arena for some time to habituate and explore their environment and were trained on trails that were short and not necessarily Y-trails.

4.2.3 Task

The table was cleaned before every trial. The trails were drawn with odorized wax crayons [45] which contain methyl salicylate in mineral oil. At random positions on the trails, small pieces of food (such as peanut or chocolate) were placed as a reward for the mice to keep them motivated. The location and shapes of the trails were different from one trial to the other. However, two types of Y-trails were included, symmetric trails that branched at somehow equal angles, and asymmetric trails that branched at very different angles.

4.2.4 Video Analysis

63 trials were analyzed where each trial ran for approximately 3 minutes and the mouse was presented with a different trail (so total of 63 trails). Optimouse open source [6] was used to extract the body and nose positions from the raw files (done by Andrew Papale in Nathan Urban's lab). The missing data found in the positions were filled using the 'fillgaps' function in matlab which performs forward and reverse autoregressive fits of the intact data to extrapolate an estimate new position arrays. The missing data occurred mainly on the edge of the arena where the mouse could not be detected by the camera from below. One can simply remove the missing data altogether but we decided on replacing them in the body and nose positions which are needed for subsequent computations. In some of the figures below, we do end up removing the data where the mouse hangs at the edge.

4.2.5 Behavioral Analysis

We first started by extracting information about the trails such as the endpoints position, branching point position, three different branches, angles between the branches and we accordingly characterize the Y trail as either symmetric or asymmetric. Symmetric trails are when the branches bifurcate at similar angles while asymmetric trails have branches with more acute angles. We characterized the angles such that if $\alpha_1 > \alpha_2 > \alpha_3$ then α_1 was labeled as least acute, α_2 as acute and α_3 as most acute (Fig. 34 left panel).

Each trial was split into stretches of trail following. We defined trail following as being at a maximum distance of 10cm from the trail for $n = 40$ consecutive frames (Fig. 32).

We used the adaptive windowing Janabi-Sharifi algorithm (window size = 50 and an error term = 0.2) [34], modified by Andrew Papale to allow for post-smoothing of 0.1 seconds, to calculate the derivatives.

We calculated the average velocities of both the body and the nose of the mice when they were in the trail following phase (Fig. 33).

We found that in many trail following stretches mice transitioned from one branch to another. For each transition, we found the angle of the branch that the mouse chose and computed the probability of a branch being visited from the other two branches (Fig. 34).

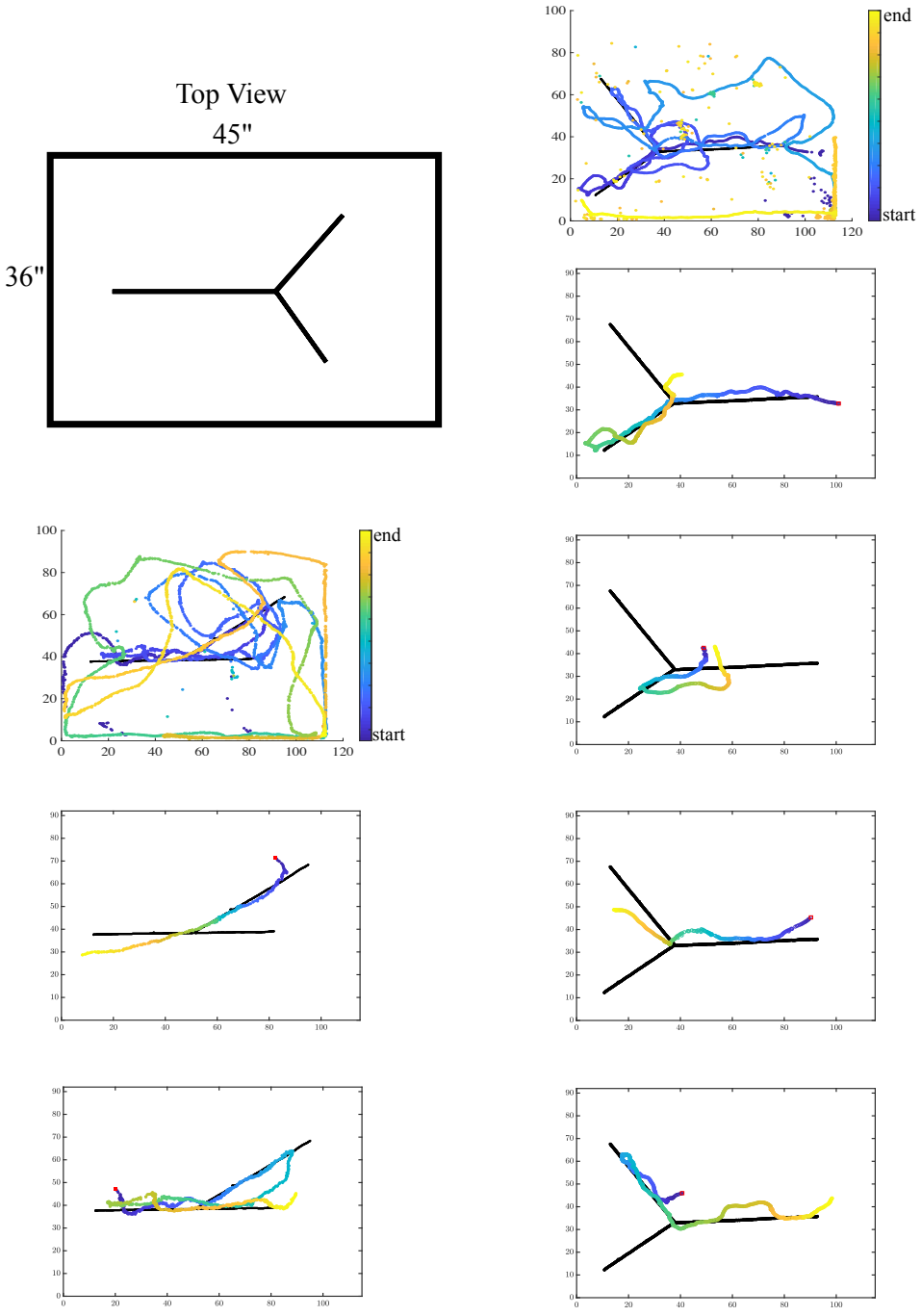

Figure 32: Examples of Mice Trajectories on Y-trails. The top left panel is a schematic of the top view of the arena. The bottom left three panels show the complete trajectory of a mouse on an asymmetric Y-trail and two isolated instants from the same trial where the mouse is considered following the trail. The right panels show the complete trajectory of a mouse on a symmetric Y-trail and four isolated instants from the same trial where the mouse is considered following the trail.

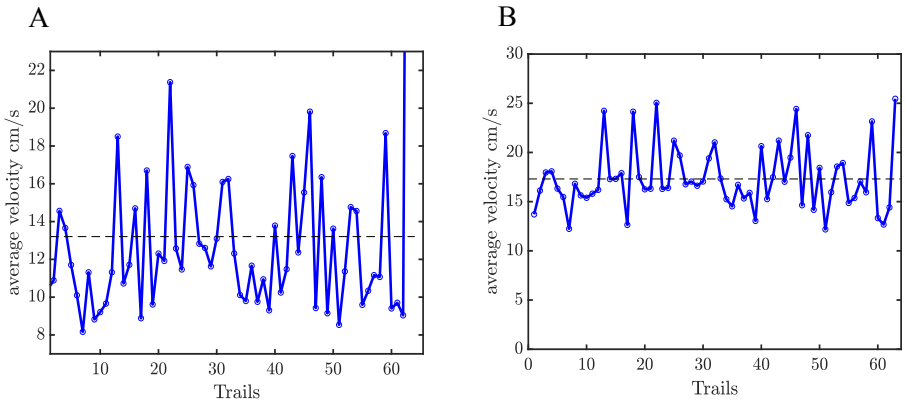

Figure 33: (A) Average body velocity for all trials when mice are following the trail. (B) Average nose velocity for all trials when mice are following the trail. (A,B) The dashed line is the average across all trials.

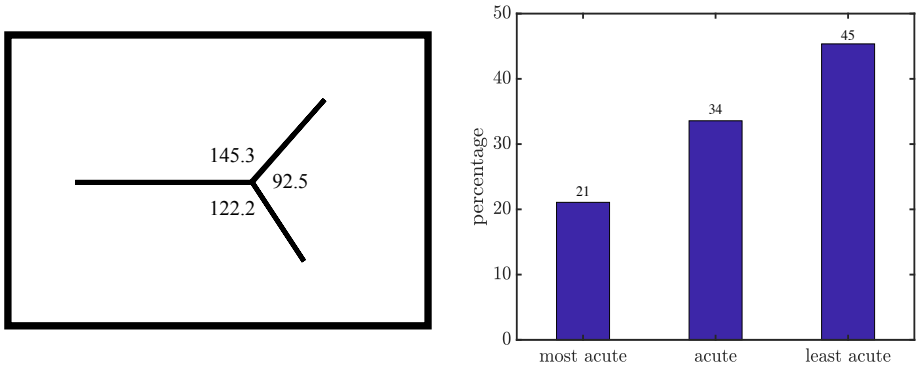

Figure 34: Left panel, schematic of Y-trail with angles between branches calculated. angle 145.3 is considered the least acute, angle 122.2 is considered the acute, angle 92.5 is considered the most acute. Right panel, Percentage of branch chosen when mice navigate from one branch to another.

To calculate the percentage of arena explored, we binned the arena into 10000 bins for every trial and excluded $4cm$ from each edge because the mice usually spend a big part of the trial hanging around the edges (Fig. 35D).

We determined the occupancy ratio, Fig. 35C, by finding the shortest distance between the data points and the trails and then partitioning the distance into 2cm blocks. We then counted the data points that belong in this partition and divided by all the samples that were not excluded (edges were again excluded here).

Using Janabi-Sharifi algorithm, we calculated the velocity vectors. For each trial, we grouped the samples that belong to the same distance away from the trail and averaged their velocities. Then we averaged across trials to get Fig. 35A for body velocities and Fig. 36A for nose velocities.

We got Fig. 35B in the same way as Fig. 35A but here instead of velocities, we looked at casting or tortuosity. To quantify this measure, we take the absolute value of the derivative of the turning angle ($d\phi = \arctan(\frac{dy}{dx})$) and divide it by the velocity, $\frac{|d\phi|}{V}$, then take $\log_{10}$. We computed the casting of the nose in Fig. 36B.

4.2.6 Model

We used the model from Chapter 3 where a Hill function was applied to the left and right concentrations with $c_{min} = 0.5$. Constant noise = 0.7 was added to the heading angle θ of the model. The sensor length was set to l = 5cm and the sensor angle $\phi = 0.05$ to mimic the very small distance between the nostrils of the mouse. The concentration was Gaussian with $\sigma = 2$. We set the velocity to be constant throughout the simulation at 13 cm/sec which is the average body velocity across trials when the mice are following the odor trails. We increased the sensitivity measure of the concentration difference β to 40 and we set $dt = 0.01$ which is not realistic to the mouse which sniffs at a rate 0.1. Also, we allowed for reflective boundaries such that the mouse reflects at an angle = π when its nares hit the walls.

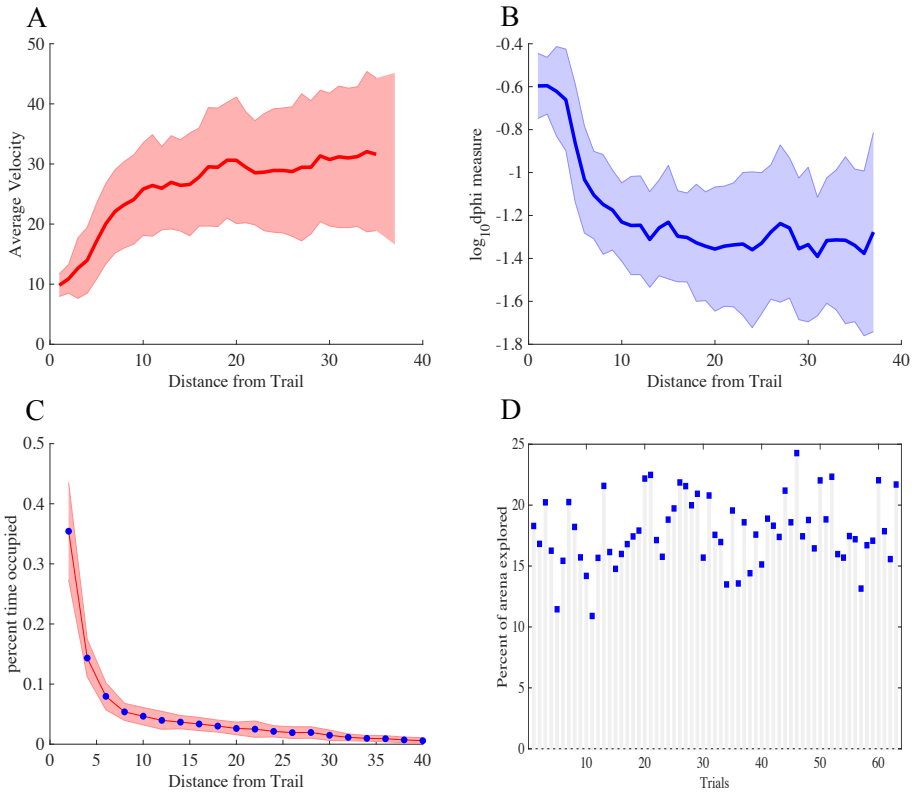

Figure 35: (A) Average body velocity across trials binned by distance to the trail. (B) Tortuosity measure of the body across trials binned by distance to the trail. (C) Ratio of time occupied across trials at a specific distance from trail. (A,B,C) Shaded area is the standard deviation of the values across trials. (D) Percent of arena explored at each trial.

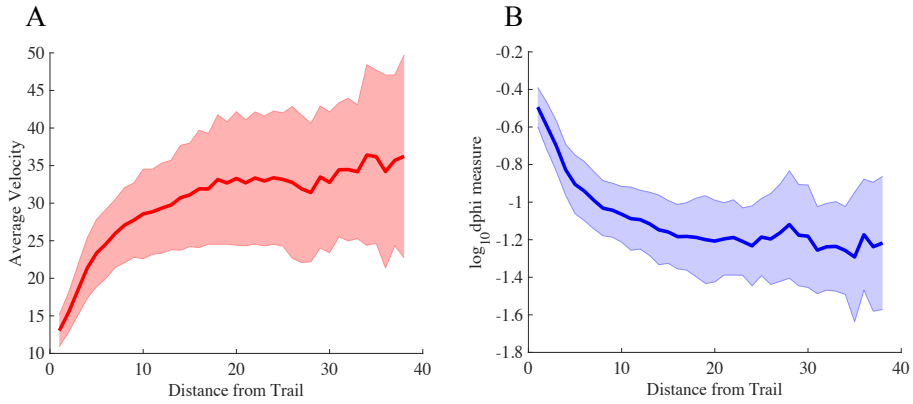

Figure 36: (A) Average nose velocity across trials binned by distance to the trail. (B) Tortuosity measure of the nose across trials binned by distance to the trail. (A,B) Shaded area is the standard deviation of the values across trials.

4.3 Results

The results discussed next are preliminary.

4.3.1 Mice Follow the Trail

From Fig. 32, we observe that the mice favor staying on the edge of the arena but that does not mean that they do not try to follow the trail. Mice are trained on this task and the trails are randomly baited with small bits of food (peanut or chocolate) which motivate the mice to engage in the task. When we split the whole trial into stretches of samples where the mouse is < 10 cm from the trail (i.e. following the trail by our definition), we find that the mouse does not randomly stay next to the trail but it actually follows it.

We examine whether the mice are exploring the arena by binning the arena and removing the data within 4cm of the edges. Fig. 35D shows that mice explore between $11 - 25\%$ of the arena which indicates that the animals are either around the trail or on the edges. This might be due to the size of the trails relative to the arena which means that the mice are able to detect where the trail is even from the walls.

4.3.2 Mice Modulate Their Behavior As a Function of Distance From Odor Trail

To further check whether the mice are spending time following the trail, we look at the ratio of time spent as a function of distance from the odor. We notice from Fig. 35C that the mice spend a majority of the experiment around the trail. They spend $\approx 67\%$ of the time (excluding time they are on the walls) at a distance < 10 cm from trail. Once the distance from the trail increases, this figure shows that the mouse spends less time at these locations. This again demonstrates that the mice are not exploring the arena but are either on the wall or around the trail.

At every stretch, we calculated the average body and nose velocities in Fig. 33. From Fig. 33A, the average body velocity ranges between $8 - 22$ cm/sec except for the last trial and the average nose velocity ranges between $12 - 25$ cm/sec as seen in Fig. 33B. Across all trials, the average body velocity = 13.204 cm/sec and the average nose velocity = 17.3 cm/sec. This is consistent with values from other studies (such as [45]) where the nose is usually faster than the body because of its sweeps and are in a range that indicates they are actively following the trail. This is further affirmed in Fig. 35A and 36A. We find that as the mice move towards the odor trail, their average velocities across trials decrease and the variation decreases. This suggests that the mice are perceiving a higher intensity of the concentration and they are changing their strategy and behavior to incorporate this concentration change. We also note that at around 10cm the body velocity has a sharper change in its magnitude and at around 15cm the nose velocity has a sharper change. We need to further investigate if this is because of our data or if this will remain true when more trails are analyzed. One reason might be that at such distance, the odor concentration is crossing a threshold that the mice are using to switch strategies.

From Fig. 35B and 36B, we observe that the opposite occurs for the casting of both body and nose. Here, as the mice move closer to the odor source and around 10cm from the trail, we observe a sharp increase in the the casting magnitude suggesting that the mice are increasing body and nose sweeps when odor concentration increases. The measure of casting here divides $d\phi$ by the linear velocity therefore biasing the casting measure to the velocity

response.

4.3.3 Mice Choose the Smoother Angle

From the stretches that we calculated before, we see that when the mice are following the trail, they transition from one branch to the other. In Chapter 2, when using bilateral information on its own, we find that the model always chooses the straighter branch. This is also shown in rats [41] where they choose the straighter branch of the bifurcated trail. To be able to study whether this is observed in mice too, we calculate the angles between the branches and accordingly categorize which angle the mice choose in order to move to the next branch. We see from the right panel of Fig. 34 that mice favor the smoother angle as well (least acute). Two things we should note: first the number of symmetric trails, where the least acute and acute angle are very close to each other, outnumber the asymmetric trails in this dataset. Second, we think that more trails need to be analyzed in order to confidently proclaim this as a pattern of behavior by the mice.

4.3.4 Simple Model Behavior

When we use the model we specified in the Methods, we find that the agent is able to follow trails. From Fig. 37, we see that on both symmetric and asymmetric trails, the model is successful in following the trail and transitioning from one branch to another. The stretches of trail following are not exhaustive for we observe stretches, similar to mice, where the agent either starts on a trail and then leaves it or does not choose a branch but keeps on straight. After we allow the agent to reflect of the walls, we see some bouncing around the edges in the first row figures in Fig. 37, but do not consider this behavior as spending time on the edges. Therefore, when we calculate the percent of arena explored with the trajectories obtained from the model in Fig. 38B, we do not remove any data points. Still, the model explores $10-20\%$ of the arena which is similar to the $11-25\%$ we get with mice trajectories.

In Fig. 38A, the percentage of branch chosen which is calculated from the model trajectories are comparable to the results we get with the mice. The model chooses the most

acute branch, fewer than the mice, in favor for the acute angle which is justifiable because there are more symmetric trails.

4.4 Discussion

In the arena, mice either hang around the edges or are around the trail without exploring other parts of the arena. As the mouse heads towards the trail, it modulates its velocity and casting such that at distance around 10cm from the trail, the velocity sharply decreases and the casting sharply increases. We want to further study this threshold and understand the reason and advantage of increasing casting. Is casting similar to the noise we added in Chapter 3 where there is an optimal amplitude that improves the performance even next to the source?

The model, though simple, performs well in following the trails especially that the boundaries are reflecting and thus the trajectories do not leave the arena. We still want to study how changing the parameters affect the model behavior. In the future, we also want to introduce different strategies to the model to better determine what cues are most useful to the mouse. Such strategies might be concentration dependent velocity which occurs in mice data. Another strategy would be introducing casting to the model and either modulating it by the velocity or the concentration.

We find that in both the mice and model trajectories, straighter branches (or smoother angles) are chosen over more acute angles. We are not sure if the results using the model are due to the effect of the bilateral term, the noise or even how the concentration is defined at the branching point. However, it would be interesting to pin down if the bilateral term is behind this result in both the model and the mice.

We are also interested in what is happening around the branch point to maybe understand how the mice choose one branch over the other. Does the velocity further decrease around the

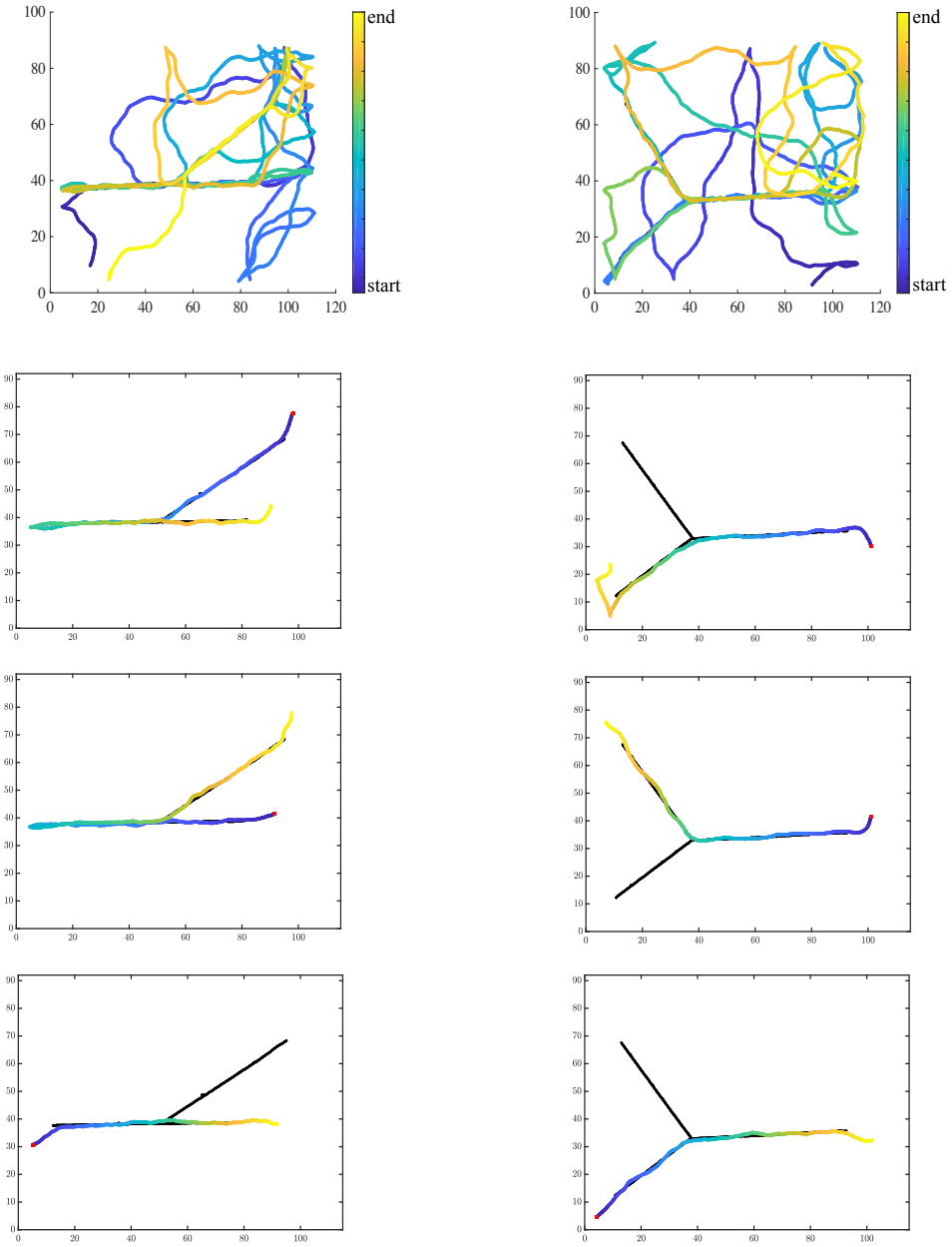

Figure 37: The left panels show the complete trajectory of the model on the same asymmetric Y-trail from Fig. 32 and stretches of trail following. The right panels show the complete trajectory of a model on a symmetric Y-trail and stretches of trail following.

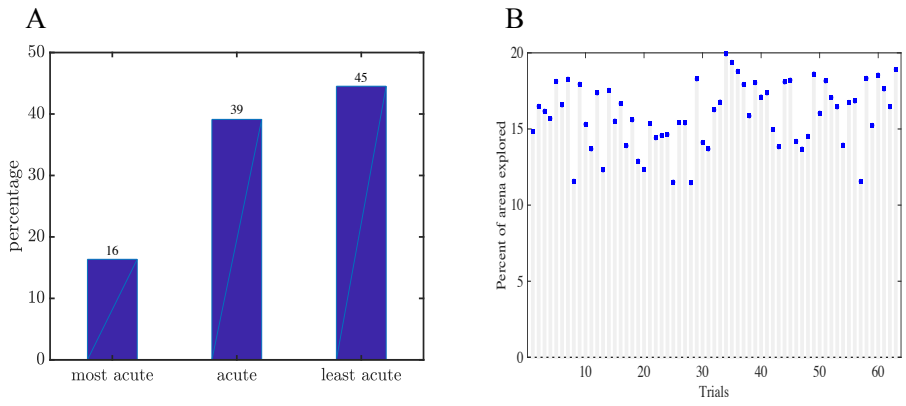

Figure 38: Behavior of the model. (A) Percentage of branch chosen when model navigate from one branch to another. (B) Percent of arena explored at each simulation.

branch point or does casting increase in an attempt by the mouse to gather more information and then decide? Is the nose closer to one branch and thus leading the mouse to choose that branch? In mice, one would expect that a swinging nose (casting) might cause the branches to be equally chosen according to which branch the nose is closer to at the time. We want to examine if mice are integrating memory or choosing ahead where they are orienting. We hope we will be able to understand and answer these questions in the future.

5.0 Conclusion

Olfaction is a sensory modality that is not very well studied. Although research has picked up in the last decade or two in studying olfaction and olfactory navigation, there is still a lot that we need to learn. This is due to the different aspects of olfactory navigation that are complex. The odor landscape itself is usually turbulent and not easily described. Throughout the experiments and modeling, we can not exactly quantify the odor concentration that the animals are perceiving. Though we observe and analyze odor driven behaviors, we are also not sure what rules or strategies are governing these behaviors. Moreover, the neural circuitry that underlie odor perceptions and translate them into actions is still a challenge to understand. However, this should not dissuade us from continuing to investigate all facets of olfactory navigation whether it is plume structure, neurological processes, animal behavior analysis or mathematical modeling of algorithms and behavior. In this dissertation, we analyzed behavior of mice performing an odor tracking task. We used mathematical modeling to further our understanding of animal behavior, the algorithm that uses bilateral information, and the effect of noise on the performance of the model and maybe the animal.

In chapter two, we analyzed a simple model that employs bilateral information to navigate odor sources. We studied its behavior in the presence of infinite and circular trails and one or more point sources. We find that for the spot source, the stable manifold of the saddle point acts like a basin of attraction such that any time the agent starts above this manifold, it navigates toward the spot source. When an infinite line is presented, the system exhibits only stable fixed points but still has a basin of attraction around the trail so that only when the agent is inside this region it can follow the trail. In both cases, the basin of attraction is affected by the parameters of the model; however, if the agent start outside of this basin, it will never find the source. This indicates that bilateral information is useful as a local algorithm when it is not paired by any other strategy.

In chapter three, we add on the bilateral model some noise and investigate whether its

performance will remain constrained by the basin of attraction. We find that adding noise to the heading angle is always beneficial in the presence of a spot source whether this noise is constant or concentration dependent.There is always an optimal level of noise that maximizes the success rate. The ability to successfully find a source becomes less constrained by the basin of attraction (as seen the deterministic case) and more dependent on the distance to source. This improvement is notable when a Hill function is added. The Hill function is significant for its role as the first step in olfaction due to the relationship between the receptors and odor concentrations. We also observe that for concentration dependent noise, the performance is optimized when the noise acts as a switch that turns off once a small amount of concentration is detected. This is in contrast to what has been shown in chapter three where mice become more tortuous in higher concentrations. On the infinite line, concentration dependent noise is not useful and a small constant noise can peak the success rate at high values.

In the final chapter, we analyzed mice behavior on bifurcated trails. We find that mice are able to track the odor trail without any exploration of the other parts of the arena. We also see that mice tend to choose smoother angles in bifurcated trails. However, we are careful not to form a conclusion before further studying and understanding the behavior before and around the branching point. We observe that many patterns of behavior in mice change and are modulated by the distance to the trail which is a substitute of concentration intensity. We find that the velocity and casting have a sharp change in their values when the mice get within 10 cm of the trail. Moreover, we see that the model from chapter 3, with different parameters, can perform the task of odor tracking. In the future, we want to try and better understand whether a change in strategies in mice is responsible for the change in behavioral patterns. We also want to further develop a model that better describes the strategies the mice are using here.

Bibliography

[1] Álvarez-Salvado, E., Licata, A. M., Connor, E. G., McHugh, M. K., King, B. M., Stavropoulos, N., Victor, J. D., Crimaldi, J. P., and Nagel, K. I. Elementary sensory-motor transformations underlying olfactory navigation in walking fruit-flies. *Elife 7* (2018), e37815.

[2] Amo, L., Galván, I., Tomás, G., and Sanz, J. J. Predator odour recognition and avoidance in a songbird. *Functional Ecology 22*, 2 (2008), 289–293.

[3] Baker, K. L., Dickinson, M., Findley, T. M., Gire, D. H., Louis, M., Suver, M. P., Verhagen, J. V., Nagel, K. I., and Smear, M. C. Algorithms for olfactory search across species. *Journal of Neuroscience 38*, 44 (2018), 9383–9389.

[4] Bartumeus, F., da Luz, M. G. E., Viswanathan, G. M., and Catalan, J. Animal search strategies: a quantitative random-walk analysis. *Ecology 86*, 11 (2005), 3078–3087.

[5] Beglane, P. F., Grasso, F. W., Basil, J. A., and Atema, J. Far field chemo-orientation in the american lobster, homarus americanus: Effects of unilateral ablation and lesioning of the lateral antennule. *The Biological Bulletin 193*, 2 (1997), 214–215. PMID: 28575588.

[6] Ben-Shaul, Y. Optimouse: a comprehensive open source program for reliable detection and analysis of mouse body and nose positions. *BMC biology 15*, 1 (2017), 1–22.

[7] Boie, S. D., Connor, E. G., McHugh, M., Nagel, K. I., Ermentrout, G. B., Crimaldi, J. P., and Victor, J. D. Information-theoretic analysis of realistic odor plumes: What cues are useful for determining location? *PLOS Computational Biology 14*, 7 (07 2018), 1–19.

[8] Bonadonna, F., and Bretagnolle, V. Smelling home: a good solution for burrow-finding in nocturnal petrels? *Journal of Experimental Biology 205*, 16 (2002), 2519–2523.

[9] Borst, A., and Heisenberg, M. Osmotropotaxis indrosophila melanogaster. *Journal of comparative physiology 147*, 4 (Dec 1982), 479–484.

[10] Bovet, P., and Benhamou, S. Spatial analysis of animals' movements using a correlated random walk model. *Journal of theoretical biology 131*, 4 (1988), 419–433.

[11] Buitron, D., and Nuechterlein, G. L. Experiments on Olfactory Detection of Food Caches by Black-Billed Magpies. *The Condor 87*, 1 (02 1985), 92–95.

[12] Calenbuhr, V., Chrétien, L., Deneubourg, J.-L., and Detrain, C. A model for osmotropotactic orientation (ii). *Journal of Theoretical Biology 158*, 3 (1992), 395 – 407.

[13] Calenbuhr, V., and Deneubourg, J.-L. A model for osmotropotactic orientation (i). *Journal of Theoretical Biology 158*, 3 (1992), 359 – 393.

[14] Calhoun, A. J., Chalasani, S. H., and Sharpee, T. O. Maximally informative foraging by caenorhabditis elegans. *Elife 3* (2014), e04220.

[15] Catania, K. C. Stereo and serial sniffing guide navigation to an odour source in a mammal. *Nature Communications 4* (02 2013), 1441.

[16] Catania, K. C. All in the family –touch versus olfaction in moles. *The Anatomical Record 303*, 1 (2020/09/28 2020), 65–76.

[17] Codling, E. A., Plank, M. J., and Benhamou, S. Random walk models in biology. *Journal of the Royal society interface 5*, 25 (2008), 813–834.

[18] Connor, E. G., McHugh, M. K., and Crimaldi, J. P. Quantification of airborne odor plumes using planar laser-induced fluorescence. *Experiments in Fluids 59*, 9 (Aug 2018), 137.

[19] Conover, M. R. *Predator-prey dynamics: the role of olfaction*. CRC Press, 2007.

[20] Crimaldi, J. Planar laser induced fluorescence in aqueous flows. *Experiments in fluids 44*, 6 (2008), 851–863.

[21] Dees, N. D., Bahar, S., and Moss, F. Stochastic resonance and the evolution of daphnia foraging strategy. *Physical Biology 5*, 4 (2008), 044001.

[22] Deneubourg, J.-L., Pasteels, J. M., and Verhaeghe, J.-C. Probabilistic behaviour in ants: a strategy of errors? *Journal of theoretical Biology 105*, 2 (1983), 259–271.

[23] Derby, C., Steullet, P., J Horner, A., and Cate, H. The sensory basis to feeding behavior in the caribbean spiny lobster panulirus argus. *Mar. Freshwater Res 52* (01 2001), 1339–50.

[24] Døving, K. B., Stabell, O. B., Östlund-Nilsson, S., and Fisher, R. Site fidelity and homing in tropical coral reef cardinalfish: are they using olfactory cues? *Chemical Senses 31*, 3 (2006), 265–272.

[25] Draft, R. W., McGill, M. R., Kapoor, V., and Murthy, V. N. Carpenter ants use diverse antennae sampling strategies to track odor trails. *Journal of Experimental Biology 221*, 22 (2018).

[26] Duistermars, B. J., Chow, D. M., and Frye, M. A. Flies require bilateral sensory input to track odor gradients in flight. *Current Biology 19*, 15 (2009), 1301 – 1307.

[27] Freund, J. A., Schimansky-Geier, L., Beisner, B., Neiman, A., Russell, D. F., Yakusheva, T., and Moss, F. Behavioral stochastic resonance: how the noise from a daphnia swarm enhances individual prey capture by juvenile paddlefish. *Journal of Theoretical Biology 214*, 1 (2002), 71–83.

[28] Gorur-Shandilya, S., Demir, M., Long, J., Clark, D. A., and Emonet, T. Olfactory receptor neurons use gain control and complementary kinetics to encode intermittent odorant stimuli. *Elife 6* (2017), e27670.

[29] Grasso, F. W., and Basil, J. A. How lobsters, crayfishes, and crabs locate sources of odor: current perspectives and future directions. *Current Opinion in Neurobiology 12*, 6 (2002), 721 – 727.

[30] Greenwood, P. E., Ward, L. M., Russell, D. F., Neiman, A., and Moss, F. Stochastic resonance enhances the electrosensory information available to paddlefish for prey capture. *Physical Review Letters 84*, 20 (2000), 4773.

[31] Hangartner, W. Spezifität und inaktivierung des spurpheromons von lasius fuliginosus latr. und orientierung der arbeiterinnen im duftfeld. *Zeitschrift für vergleichende Physiologie 57*, 2 (Jun 1967), 103–136.

[32] Hills, T. T., Todd, P. M., Lazer, D., Redish, A. D., Couzin, I. D., Group, C. S. R., et al. Exploration versus exploitation in space, mind, and society. *Trends in cognitive sciences 19*, 1 (2015), 46–54.

[33] Jackson, J., Webster, D., Rahman, S., and Weissburg, M. Bed roughness effects on boundary-layer turbulence and consequences for odor-tracking behavior of blue crabs (callinectes sapidus). *Limnology and Oceanography 52*, 5 (2007), 1883–1897.

[34] Janabi-Sharifi, F., Hayward, V., and Chen, C.-S. J. Novel adaptive discrete-time velocity estimation techniques and control enhancement of haptic interfaces. *IEEE Trans. Control Systems Technology 8*, 6 (2000), 1003–1009.

[35] Jinn, J., Connor, E., and Jacobs, L. F. How ambient environment influences olfactory orientation in search and rescue dogs. *Chemical Senses* (09 2020). bjaa060.

[36] Jinn, J., Connor, E. G., and Jacobs, L. F. How ambient environment influences olfactory orientation in search and rescue dogs. *Chemical senses 45*, 8 (2020), 625–634.

[37] Jones, P. W., and Urban, N. N. Mice follow odor trails using stereo olfactory cues and rapid sniff to sniff comparisons. *BioRxiv* (2018), 293746.

[38] Justus, K. A., Murlis, J., Jones, C., and Cardé, R. T. Measurement of odor-plume structure in a wind tunnel using a photoionization detector and a tracer gas. *Environmental Fluid Mechanics 2*, 1 (2002), 115–142.

[39] Kelley, J. L., and Magurran, A. E. Learned predator recognition and antipredator responses in fishes. *Fish and Fisheries 4*, 3 (2003), 216–226.

[40] Kennedy, J. S., and Marsh, D. Pheromone-regulated anemotaxis in flying moths. *Science 184*, 4140 (1974), 999–1001.

[41] Khan, A. G., Sarangi, M., and Bhalla, U. S. Rats track odour trails accurately using a multi-layered strategy with near-optimal sampling. *Nature Communications 3* (02 2012), 703.

[42] Kikuta, S., Sato, K., Kashiwadani, H., Tsunoda, K., Yamasoba, T., and Mori, K. Neurons in the anterior olfactory nucleus pars externa detect right or left localization of odor sources. *Proceedings of the National Academy of Sciences 107*, 27 (2010), 12363–12368.

[43] Kuenen, L., and Carde, R. T. Strategies for recontacting a lost pheromone plume: casting and upwind flight in the male gypsy moth. *Physiological Entomology 19*, 1 (1994), 15–29.

[44] Leonard, A. E., Voigt, R., and Atema, J. Lobster orientation in turbulent odor plumes: Electrical recording of bilateral olfactory sampling (antennular "flicking"). *The Biological Bulletin 187*, 2 (1994), 273–273. PMID: 7811822.

[45] Liu, A., Papale, A. E., Hengenius, J., Patel, K., Ermentrout, B., and Urban, N. N. Mouse navigation strategies for odor source localization. *Frontiers in Neuroscience 14* (2020), 218.

[46] Louis, M., Huber, T., Benton, R., Sakmar, T. P., and Vosshall, L. B. Bilateral olfactory sensory input enhances chemotaxis behavior. *Nature Neuroscience 11* (12 2007), 187 EP –.

[47] MARTIN, H. Osmotropotaxis in the honey-bee. *Nature 208*, 5005 (1965), 59–63.

[48] McDonnell, M. D., and Abbott, D. What is stochastic resonance? definitions, misconceptions, debates, and its relevance to biology. *PLoS computational biology 5*, 5 (2009), e1000348.

[49] Means, L. W., Alexander, S. R., and O'Neal, M. F. Those cheating rats: male and female rats use odor trails in a water-escape "working memory" task. *Behavioral and neural biology 58*, 2 (1992), 144–151.

[50] Moore, P., and Crimaldi, J. Odor landscapes and animal behavior: tracking odor plumes in different physical worlds. *Journal of marine systems 49*, 1-4 (2004), 55–64.

[51] Moss, F., Ward, L. M., and Sannita, W. G. Stochastic resonance and sensory information processing: a tutorial and review of application. *Clinical neurophysiology 115*, 2 (2004), 267–281.

[52] Nagel, K. I., and Wilson, R. I. Biophysical mechanisms underlying olfactory receptor neuron dynamics. *Nature neuroscience 14*, 2 (2011), 208–216.

[53] Nosal, A. P., Chao, Y., Farrara, J. D., Chai, F., and Hastings, P. A. Olfaction contributes to pelagic navigation in a coastal shark. *PLOS ONE 11*, 1 (01 2016), 1–17.

[54] Page, J. L., Dickman, B. D., Webster, D. R., and Weissburg, M. J. Getting ahead: context-dependent responses to odorant filaments drive along-stream progress during odor tracking in blue crabs. *Journal of Experimental Biology 214*, 9 (2011), 1498–1512.

[55] Perna, A., Granovskiy, B., Garnier, S., Nicolis, S. C., Labédan, M., Theraulaz, G., Fourcassié, V., and Sumpter, D. J. Individual rules for trail pattern formation in argentine ants (linepithema humile). *PLoS computational biology 8*, 7 (2012), e1002592.

[56] Porter, J., Anand, T., Johnson, B., Khan, R. M., and Sobel, N. Brain mechanisms for extracting spatial information from smell. *Neuron 47*, 4 (2005), 581 – 592.

[57] Porter, J., Craven, B., Khan, R. M., Chang, S.-J., Kang, I., Judkewitz, B., Volpe, J., Settles, G., and Sobel, N. Mechanisms of scent-tracking in humans. *Nature Neuroscience 10* (12 2006), 27.

[58] Rabell, J. E., Mutlu, K., Noutel, J., Del Olmo, P. M., and Haesler, S. Spontaneous rapid odor source localization behavior requires interhemispheric communication. *Current Biology 27*, 10 (2017), 1542–1548.

[59] Rafferty, N. E., and Boughman, J. W. Olfactory mate recognition in a sympatric species pair of three-spined sticklebacks. *Behavioral Ecology 17*, 6 (2006), 965–970.

[60] Rajan, R., Clement, J. P., and Bhalla, U. S. Rats smell in stereo. *Science 311*, 5761 (2006), 666–670.

[61] Reeder, P. B., and Ache, B. W. Chemotaxis in the florida spiny lobster, panulirus argus. *Animal Behaviour 28*, 3 (1980), 831 – 839.

[62] Riman, N., Victor, J. D., Boie, S. D., and Ermentrout, B. The dynamics of bilateral olfactory search and navigation. *SIAM Review 63*, 1 (2021), 100–120.

[63] Russell, D. F., Wilkens, L. A., and Moss, F. Use of behavioural stochastic resonance by paddle fish for feeding. *Nature 402*, 6759 (1999), 291–294.

[64] Ruther, J., Reinecke, A., Thiemann, K., Tolasch, T., Francke, W., and Hilker, M. Mate finding in the forest cockchafer, melolontha hippocastani, mediated by volatiles from plants and females. *Physiological Entomology 25*, 2 (2000), 172–179.

[65] Rutkowski, A. J., Quinn, R. D., and Willis, M. A. Three-dimensional characterization of the wind-borne pheromone tracking behavior of male hawkmoths, manduca sexta. *Journal of Comparative Physiology A 195*, 1 (2009), 39–54.

[66] Schneirla, T. C. A unique case of circular milling in ants, considered in relation to trail following and the general problem of orientation. *American Museum Novitates*, 1253 (1944), 1–26.

[67] Steck, K. Just follow your nose: homing by olfactory cues in ants. *Current opinion in neurobiology 22*, 2 (2012), 231–235.

[68] Steck, K., Hansson, B. S., and Knaden, M. Smells like home: Desert ants, cataglyphis fortis, use olfactory landmarks to pinpoint the nest. *Frontiers in Zoology 6*, 1 (2009), 1–8.

[69] Steck, K., Knaden, M., and Hansson, B. S. Do desert ants smell the scenery in stereo? *Animal Behaviour 79*, 4 (2010), 939–945.

[70] Takasaki, T., Namiki, S., and Kanzaki, R. Use of bilateral information to determine the walking direction during orientation to a pheromone source in the silkmoth bombyx mori. *Journal of Comparative Physiology A 198*, 4 (2012), 295–307.

[71] Thesen, A., Steen, J. B., and Doving, K. Behaviour of dogs during olfactory tracking. *Journal of Experimental Biology 180*, 1 (1993), 247–251.

[72] van Breugel, F., and Dickinson, M. H. Plume-tracking behavior of flying drosophila emerges from a set of distinct sensory-motor reflexes. *Current Biology 24*, 3 (2014), 274–286.

[73] Van Cruyningen, I., Lozano, A., and Hanson, R. Quantitative imaging of concentration by planar laser-induced fluorescence. *Experiments in Fluids 10*, 1 (1990), 41–49.

[74] Vergassola, M., Villermaux, E., and Shraiman, B. I. 'infotaxis' as a strategy for searching without gradients. *Nature 445*, 7126 (2007), 406.

[75] Vickers, N. Mechanisms of animal navigation in odor plumes. *The Biological Bulletin 198*, 2 (2018/06/25 2000), 203–212.

[76] Victor, J. D., Boie, S. D., Connor, E. G., Crimaldi, J. P., Ermentrout, G. B., and Nagel, K. I. Olfactory navigation and the receptor nonlinearity. *Journal of Neuroscience 39*, 19 (2019), 3713–3727.

[77] Wallace, D. G., Gorny, B., and Whishaw, I. Q. Rats can track odors, other rats, and themselves: implications for the study of spatial behavior. *Behavioural brain research 131*, 1-2 (2002), 185–192.

[78] Wetmore, A. The role of olfaction in food location by the Turkey Vulture (Cathartes aura). *The Auk 82*, 4 (10 1965), 661–662.

[79] Wolf, H., and Wehner, R. Pinpointing food sources: olfactory and anemotactic orientation in desert ants, Cataglyphis fortis. *Journal of Experimental Biology 203*, 5 (03 2000), 857–868.

[80] Wu, Y., Chen, K., Ye, Y., Zhang, T., and Zhou, W. Humans navigate with stereo olfaction. *Proceedings of the National Academy of Sciences 117*, 27 (2020), 16065–16071.

[81] Zollner, P. A., and Lima, S. L. Search strategies for landscape-level interpatch movements. *Ecology 80*, 3 (1999), 1019–1030.